SYNTHESIS AND CHARACTERIZATION OF CARBON-SUPPORTED RHODIUM SULFIDE CATALYST

By

Dhrubajit Konwar

Submitted to the graduate degree program in Chemical and Petroleum Engineering and the Graduate Faculty of the University of Kansas in partial fulfilment of the requirements for the degree of Master of Science

_____

Chairperson Dr. Trung Van Nguyen

_____

Dr. Juan Bravo-Suarez

_____

Dr. Kevin Leonard

Date defended: July 10, 2015

CERTIFICATE

The Thesis Committee for Dhrubajit Konwar certifies that this is the approved version of the following thesis:

SYNTHESIS AND CHARACTERIZATION OF CARBON-SUPPORTED RHODIUM SULFIDE CATALYST

Chairperson Dr. Trung Van Nguyen

Dr. Juan Bravo-Suarez

Dr. Kevin Leonard

Date approved: July 10, 2015

ABSTRACT

Hydrogen-Bromine (H_2-Br_2) flow battery system is an attractive option for electrochemical energy storage due to its high round-trip energy conversion efficiency, high power density and storage capacity, fast kinetics of both hydrogen and bromine electrode reactions, low cost of active materials and reliability. The highly active conventional platinum (Pt) catalyst for hydrogen oxidation and reduction reactions (HOR/HER) is not stable in the corrosive HBr/Br_2 environment of the H_2-Br_2 fuel cell system. Hence, an alternative HOR/HER catalyst which is stable and highly active in HBr/Br_2 electrolyte is required. Rhodium sulfide (Rh_xS_y) catalysts supported on high surface area carbon (C) were synthesized by refluxing rhodium chloride with ammonium thiosulfate to replace the Pt catalyst in the H_2-Br_2 fuel cell system.

Rhodium sulfide catalyst is a mixture of several phases *i.e.* Rh_2S_3, Rh_3S_4 and $Rh_{17}S_{15}$ and Rh metal with Rh_2S_3 reported as a semiconductor, Rh_3S_4 and $Rh_{17}S_{15}$ as conducting semi-metals, and Rh metal reported to be unstable in HBr/Br_2 electrolyte. Thermal reduction of inactive Rh_2S_3 phase at high temperatures in inert gas atmosphere results in the transformation of Rh_2S_3 into active phases of Rh_3S_4, $Rh_{17}S_{15}$ and Rh metal. Comprehensive understanding of the equilibrium phase composition at various temperatures is critical to the optimization of the performance of the catalyst towards hydrogen oxidation and evolution. Hence, an effort was made to provide an equilibrium phase diagram of rhodium sulfide

catalyst heat treated at 650°C, 660°C, 670°C, 680°C, 690°C and 700°C by X-Ray Diffraction (XRD) analysis and Rietveld refinement.

In order to study the relationship between the equilibrium phase composition and HOR/HER activity, electrochemical active surface area (ECSA) and exchange current density (i_o) of the synthesized Rh_xS_y/C catalysts were calculated in 1 M H_2SO_4 solution using the rotating disk electrode (RDE) approach in a three-electrode electrochemical cell.

At phase equilibrium, the weight percentages (%) observed at different temperatures for Rh_2S_3, Rh_3S_4, $Rh_{17}S_{15}$ phases and Rh metal respectively were as follows, (28.4±2.9, 13.5±3.4, 58.1±1.4, 0.0 at 650°C); (26.9±2.0, 15.6±2.9, 57.5±0.9, 0.0 at 660°C), (23.6±1.2, 9.0±1.7, 67.4±3.4, 0.0 at 670°C); (21.3±1.9, 8.9±0.7, 69.8±1.3, 0.0 at 680°C); (2.3±2.3, 1±1.4, 95.9±1.8, 0.8±0.2 at 690°C) and (1.2±1.3, 1.6±1.5, 96.6±1.3, 0.6±0.2 at 700°C). The mass specific ECSAs (m^2/mg of Rh) of Rh_xS_y/C catalyst heat-treated (HT) for 3 h at 650°C, 660°C, 670°C, 680°C, 690°C and 700°C were observed to be 3.4 m^2/mg_{Rh} , 3.3 m^2/mg_{Rh}, 5.2 m^2/mg_{Rh}, 5.4 m^2/mg_{Rh}, 8.1 m^2/mg_{Rh} and 8.7 m^2/mg_{Rh} respectively. The HOR/HER exchange current densities were observed to be 0.34±0.04 mA/cm^2, 0.35±0.04 mA/cm^2, 0.41±0.02 mA/cm^2, 0.43±0.03 mA/cm^2, 0.57±0.06 mA/cm^2 and 0.59±0.06 mA/cm^2 for Rh_xS_y/C catalysts HT at 650°C, 660°C, 670°C, 680°C, 690°C and 700°C for 3 h respectively. The electrochemical measurements showed an increase in activity with an increase in the percentage of the active phases (Rh_3S_4 and $Rh_{17}S_{15}$) of Rh_xS_y/C catalysts which was in good agreement with the XRD results.

ACKNOWLEDGEMENT

There are a number of people without whom this thesis would not have been possible and to whom I am greatly indebted.

To my advisor Dr. Trung Van Nguyen, for his excellent guidance, moral support and motivation towards the completion of this thesis work. He showed a great deal of patience towards shaping me as an independent researcher and his faith in me and encouragement throughout have been extremely helpful to improve myself. I was impressed at his way of discussions on subject matters where he focussed on basic minute details and then proceeded to tackle the bigger issue which helped me in exploring new dimension of knowledge. Over years, Dr. Nguyen was always available in the midst of his busy schedule to discuss any technical or personal problem. I have learnt perseverance, hard work and commitment to profession from him and will be indebted to him.

To my committee members, Dr. Juan-Bravo Suarez and Dr. Kevin Leonard who were very approachable and gave excellent advice on my research.

To Dr. Victor Day of Structural Biology Centre, University of Kansas who helped me in my X-ray diffraction experiments and provided his expert opinions on crystallography.

To my colleagues, Dr. Venkata R Yarlagadda, Regis Dowd and Yuanchao Li for their guidance and lively company in lab and former colleague, Dr. Jahangir Masud for helping me with the catalyst synthesis set-up, Thank you all for the stimulating discussions and for all the fun we have had in these two years.

To Nirala Singh of the University of California, Santa Barbara, with whom I had lively discussions while learning GSAS-II software.

To the School of Engineering, University of Kansas for providing experimental resources and other latest technologies without which it would not have been possible to fulfil my objectives.

Last, certainly not the least, the love, caring and constant support and encouragement from my parents and family members back in India are invaluable assets that I got while working here in the United States. You have been always my source of inspiration.

-Dhrubajit Konwar (Dhruv).

TABLE OF CONTENTS

Chapter 2: Experimental and Computational Studies

LIST OF FIGURES

FIGURE **PAGE**

LIST OF TABLES

TABLE **PAGE**

NOMENCLATURE

a_a	anodic transfer coefficient
a_c	cathodic transfer coefficient
A	absorption factor
d	inter-planar distance (nm)
E°	standard electrochemical potential
F	Faraday constant (96487 C/mol)
F_K	structure factor for K^{th} Bragg's reflection
i	current density in A/cm^2 of geometric area
i_0	exchange current density in A/cm^2 of active area
$I_{o,i}$	observed intensity at i^{th} step
$I_{c,i}$	calculated intensity at i^{th} step
$I_{b,i}$	background intensity at i^{th} step
K	Miller indexes (hkl)
L_K	Lorentz polarization factor for K^{th} Bragg's reflection
n	integer
M	molecular weight (atomic mass units)
R	universal gas constant (8.314 J/mol K)
R_w	weighted-profile factor
S	scale factor
T	temperature (°C)
V	unit cell volume (Å^3)

W	weight fraction
Z	number of molecules in a unit cell
η	over-potential (V)
Θ	scattering angle
λ	wavelength (nm)

Abbreviations and acronyms widely used in the text

AS	aqueous synthesis
C1	Rh_xS_y/C HT at 650°C
C2	Rh_xS_y/C HT at 660°C
C3	Rh_xS_y/C HT at 670°C
C4	Rh_xS_y/C HT at 680°C
C5	Rh_xS_y/C HT at 690°C
C6	Rh_xS_y/C HT at 700°C
C1-3	Rh_xS_y/C HT at 650°C for 3h
C1-4	Rh_xS_y/C HT at 650°C for 4h
C1-5	Rh_xS_y/C HT at 650°C for 5h
CV	cyclic voltammetry
ECSA	electrochemical active surface area
HER	hydrogen evolution reaction
HOR	hydrogen oxidation reaction
HSF	hydrogen sulfide free
HS	hydrothermal synthesis
HT	heat-treated

ICDD International Centre of Diffraction Data

NA non-aqueous

OCV open circuit voltage

RDE rotating disk electrode

RHE reversible hydrogen electrode

Rh_xS_y/C rhodium sulfide supported on carbon

RT room-temperature

SCE saturated calomel electrode

SD standard deviation

XRD X-ray diffraction

CHAPTER 1
INTRODUCTION

1.1. Electrical Energy Storage

Over the last few decades, electricity generation has grown significantly. According to the report published by International Energy Agency (IEA), the annual net production of electricity was 22668 TW h out of which fossil fuels (natural gas, coal and oil) contributed around 70% of the total electricity production [1]. When we consider the increasing energy demands on dwindling fossil reserves as well as the negative impact on the environment due to CO_2 emissions, a lot of research and funding for cleaner renewable energy sources like wind and solar were made to mitigate the impact. As of 2007, global electricity production from wind was 94 GW and it is estimated to reach 474 GW by 2020 [2]. In addition, electricity generation from solar photovoltaics are growing at 40 % annually and by 2020, the United States is estimated to generate 100 GW of electricity from solar energy [2].

However, wind and solar energy are intermittent and are not reliable power sources. These energy sources have to be stored for use during night or cloudy days and for times when there is less wind. Moreover, renewable sources are localized and often far away from load centres of application. For example, in the United States, wind sources are mostly available in the mid-west region and solar energy are abundant in the south-west region on an annual scale. To account for the variability of renewable energy sources, electrical energy storage (EES) is necessary so that energy from these variable sources can be stored in a certain form, according to the technology used, and then converted into electrical energy whenever and wherever required.

Electrochemical energy storage technology can be referred to converting energy (mainly electrical) to another form and reserving it, and later this stored energy is converted back to electrical energy whenever needed [3]. Electrical energy can be stored directly as electricity in the form of capacitors, superconducting magnetic energy storage, mechanically in the form of kinetic energy (flywheels) or potential energy (pumped hydro storage and compressed air energy storage), and chemically in the form of secondary batteries, flow batteries and fuel cells.

Electrochemical energy storage *via* flow battery/reversible fuel cell devices is considered to be one of the most feasible options to store renewable energy sources and have the potential to be among the lowest cost alternatives [4]. A flow battery or redox flow battery (RFB) can be defined as an electrochemical device consisting of two electrolytes that converts the chemical energy directly into electrical energy by exchanging ions though a ion conducting membrane [5]. A schematic diagram of a redox flow battery is shown in Figure 1.1.

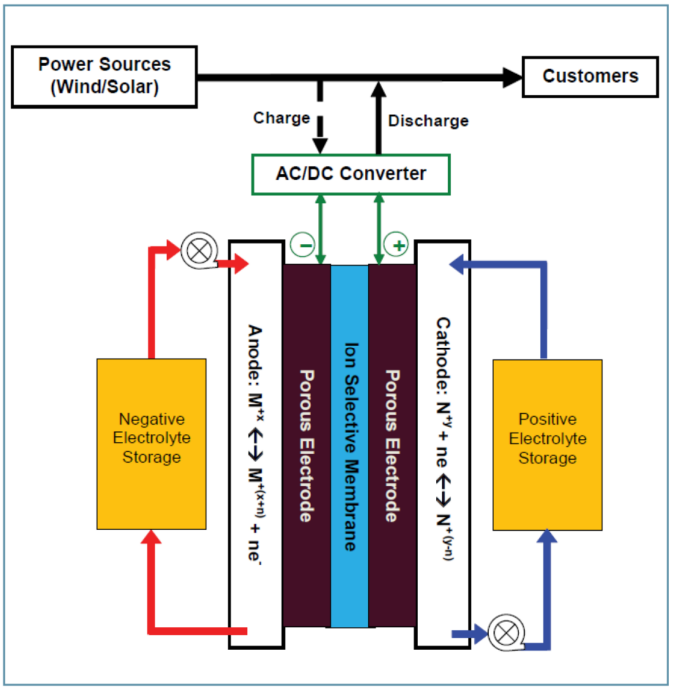

Fig. 1.1. Schematic of a redox flow battery system [5]

As shown in Figure 1.1, the electrolytes *viz.* positive electrolyte or catholyte and negative electrode or anolyte are stored in two external tanks that are pumped through the power conversion device during charging and discharging operations. During periods of high demand, the anolyte is pumped through the porous negative electrode and is oxidized at its surface, thus generating electrons (electricity) and a positively charged species. The electrons collected *via* current collectors travel through and power up the external load and then reach the positive electrode where the reactants in the positive electrolyte are reduced, creating negatively charged ions. This mode is called discharging the electrochemical cell. The ion-selective membrane allows only the negatively or positively charged ion to cross between the electrodes, termed as anion-exchange membrane or cation-exchange membrane, respectively. During periods of low demand, electrical input to the electrochemical device forces the opposite reactions to occur at each electrode. This mode is called charging the electrochemical device.

Since the electrodes do not take part in the charging and discharging mode of the cell, high charge and discharge rates do not impact the electrode structure and thus a longer cycle life can be achieved as compared to a secondary battery, where electrodes take part in the charge and discharge operations. Another advantage of a flow battery is that the energy density (determined by the reactant concentration) is separated from power density (determined by size of the electrodes). This is analogous to fuel tank size and engine size in an automobile respectively. Thus flow batteries have scale-up and durability advantages over secondary batteries. Chen *et al.* [3] reported that flow batteries can release energy continuously at a high discharge rate for up to 10 h. During the mid-1970s, in order to tackle energy crisis and the utility industry's economic problem, NASA began researching redox flow batteries to store solar and wind power [6, 7].

A flow battery can be thought as a reversible fuel cell or regenerative fuel cell, but the majority of the fuel cell chemical reactions are not reversible enough to be an efficient flow battery (such as hydrogen-oxygen fuel cell which has a high kinetic overvoltage) [5]. Thus flow batteries are generally secondary battery type and can be recharged without replacing the electroactive material in contrast to a conventional fuel cell.

Several flow battery technologies are being modified and optimized for grid-based storage and being deployed in some installations, generating power in the order of 100 kW to 10 MW [4]. The various flow battery types are introduced as follows, iron/chromium [6], bromine/polysulfide [8], all-vanadium [9], vanadium/bromine [10], zinc/bromine [11], iron/chromium [12] and hydrogen/bromine [13], *etc*. In comparison to other flow battery systems, the hydrogen/bromine fuel cell has advantages including high round-trip energy conversion efficiency, high power density and storage capacity, fast kinetics of both hydrogen and bromine electrode reactions, low cost of active materials and reliability [14-16].

1.2. Hydrogen-Bromine (H_2-Br_2) Flow Battery System

The first major study on the hydrogen bromine fuel cell was conducted by Werner and Glass [17]. Yeo and Chin investigated and reported excellent electric-to-electric efficiency, introducing H_2-Br_2 flow battery as a promising RFB system for energy storage applications [16]. NASA began focussing on the H_2-Br_2 flow battery in the mid to late 1980s [18].

The operating principle of the H_2-Br_2 RFB can be described with a typical cell structure as shown in Figure 1.2.

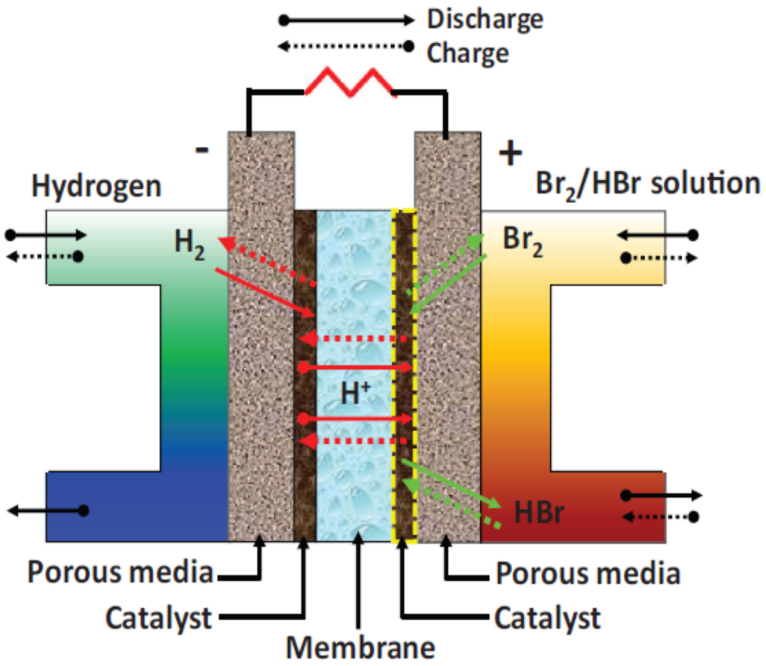

Fig.1.2. Schematic of H_2/Br_2 redox flow battery [19]

The discharge and charge reactions occurring at the cell are as follows,

Discharge mode:

At the hydrogen (negative) electrode, H_2 gas is oxidized to produce hydronium ions (H^+) and electrons,

$$\boldsymbol{H_2 \xrightarrow{discharge} \xleftarrow[charge]{} 2H^+ + 2\,e^-\ ,\qquad E^0 = 0.00\ V}$$

The electrons collected *via* current collectors travel through and power up the external load and then reach the bromine (positive) electrode where the bromine is reduced to bromide,

$$\boldsymbol{Br_2 + 2e^- \xrightarrow{discharge} \xleftarrow[charge]{} 2Br^-,\qquad E^0 = 1.09\ V}$$

The hydronium ions (H^+) produced at the hydrogen electrode migrate across the proton conducting membrane to the bromine side of the fuel cell and combine with the bromide ions to form hydrobromic (HBr) acid. Overall, during discharge, hydrogen (H_2) and bromine (Br_2) produces HBr and electrical output, and during charge, electrical energy input

forces the above and below reactions to occur from right to left converting HBr acid to H_2 and Br_2 as follows,

$$\boldsymbol{H_2 + Br_2 \xrightarrow[}^{discharge} \xleftarrow[charge]{} HBr + electrical\ energy\ ,} \qquad \boldsymbol{E^0 = 1.09\ V}$$

During the operation of a H_2-Br_2 fuel cell, HBr and Br_2 can cross from the bromine side to the hydrogen side through the proton conducting membrane, where Br_2 gets reduced to bromide and adsorbs onto catalyst surface, potentially leading to corrosion and poisoning of the catalyst used at the hydrogen electrode [20] . It can also react with the hydrogen directly thus leading in self-discharge of the cell. The crossover of bromide ions are more likely to occur during charge when the hydronium ions are transported from the Br_2 electrode to H_2 electrode.

Due to fast kinetics of Br_2/Br^- reaction, no precious metal is needed to catalyse the reactions at the bromine electrode [19], but the hydrogen oxidation and evolution (HOR/HER) reactions require a catalyst that should be highly stable, active and inexpensive. Moreover, the catalyst has to be stable and durable in the highly corrosive hydrobromic/bromine (HBr/Br_2) environment inside the cell. The highly active HOR/HER platinum (Pt) catalyst that is currently used is not stable in the HBr/Br_2 environment [15-21]. Consequently, an alternative HOR/HER catalyst material is required for this system.

In the recent years, there have been considerable interest in developing highly active and stable electrocatalyst by doping pure Pt with metal (Co, Ni, Cu) [22] and modifying Pt surface with metal clusters [23]. But because of major corrosion issues while employing Pt-group metals or alloys, considerable research efforts are being made in an attempt to discover more stable materials that can survive in the corrosive HBr/Br_2 environment. The majority of the proposed alternatives to platinum were based on non-noble transition metal compounds. Ivanovskaya *et al.* [24] synthesized mixed metal sulfides containing a combination of W, Fe,

Mo, Ni and Ru and established that rhodium sulfide performed better than the mixed metal sulfides in terms of HOR-HER activity and stability in HBr/Br_2 solution. Recent studies by Nguyen's group and others [15, 21] have also found rhodium sulfide catalysts to be a promising candidate for H_2-Br_2 fuel cell system due to its high stability in HBr/Br_2 environment and comparable activity.

1.3. Rhodium Sulfide Catalyst Application and Synthesis Literature Review

Rhodium sulfide electrocatalyst was first synthesized by Allen *et al.* [25], who investigated the novel catalyst for the reduction of oxygen in industrial electrolyzers. From then, rhodium sulfide catalyst has established itself as a promising candidate among transition metal chalcogenides in industries, substituting expensive and scarce platinum in hydrodesulfurization [26] and for use as oxygen reduction cathodes (ORC) for fuel cells and HCl electrolysis [27, 28].

Many synthesis methods have been reported till date to prepare carbon supported rhodium sulfide catalyst, *viz.*, aqueous synthesis process (AS) [29], non-aqueous synthesis (NA) [30] , hydrothermal synthesis (HS) [31] and H_2S gas free synthesis (HSF) [32].

In the AS process, high surface area carbon black was dispersed into a solution of rhodium trichloride. This was then followed by sulfonation of the metal moiety by bubbling a mixture of hydrogen sulfide (60 %) and nitrogen (40 %) gas. After vacuum filtering with sufficient amount of de-ionized water, and overnight drying under vacuum at 80°C, the catalyst was heat-treated in an inert gas atmosphere.

In the so called 'non-aqueous synthesis' process, rhodium carbonyl was reacted with elemental sulfur in a 3-neck flask inside an argon-filled glovebox. De-aerated xylenes were transferred along with argon gas *via*. a cannula in proportion to metal carbonyls. The system

was then refluxed under argon atmosphere at 145°C for 20 h. Carbon black was added after refluxing in proportion to achieve a 30 wt % (rhodium metal basis) loading.

The HS process involves hydrothermal reaction between rhodium carbonyl and sulfur in an autoclave at high temperature. However, the rhodium sulfide catalyst particle sizes synthesized from this method varied from 50-100 nm which made it unsuitable to be used in fuel cell applications due to low gravimetric electrochemical active surface area (ECSA) as compared to rhodium sulfide catalysts (particle size 5-20 nm) synthesized from other processes.

H_2S free synthesis is identical to the aqueous synthesis process except the sulfonation process was achieved by proportional addition of thio-containing compounds until a stable pH was reached and the solution turned colorless. The filtered and dried material was then heat treated in an inert gas atmosphere.

Although catalyst synthesized from the AS, NA and HSF processes showed good electrocatalytic performances in oxygen reduction activity [28], the production *via* AS process is affected by some inconveniences. Firstly, the use of hydrogen sulfide, which is highly flammable and noxious gas, poses serious environmental and human health issues. Also handling hydrogen sulfide gas have to be dealt with expensive equipment and safety measures. The NA synthesis involves the toxic xylene, which again leads to environmental and health hazards. Moreover, NA synthesis process yielded highly amorphous rhodium sulfide catalyst which is not favourable for HOR-HER reactions. Thus, HSF free synthesis process was preferred in our rhodium sulfide catalyst synthesis process due to its above mentioned advantages over all the processes. Detailed experimental synthesis about HSF synthesis process is discussed in Chapter 2.

1.4. Crystal Structure of Rhodium Sulfide Compounds

The first investigation to study rhodium sulfide compounds was undertaken by Juza *et al.* in 1935 [33]. They found several phases for rhodium sulfide including Rh_9S_8 which was later confirmed to be $Rh_{17}S_{15}$ by Geller [34] in 1965 to be cubic with $Pm\bar{3}m$ space group. P here refers to primitive cell with two mirror (m) planes intersecting at 3 fold rotation axes. Soon after $Rh_{17}S_{15}$ was characterized, the structure of Rh_2S_3 was determined by Parthe *et al.* [35] in 1967, which they found to be a diamagnetic semiconductor with orthorhombic space group Pbcn. Here P refers to primitive cell with glide planes along b and c cell edges and n is a glide plane along the half of a diagonal of a face. Although Juza *et al.* [33] described a rhodium sulfide phase in the form Rh_3S_4, it was Beck *et al.* [36] who first synthesized and characterized Rh_3S_4 in 2000. They found Rh_3S_4 to be a monoclinic structure with space group number C*2/m*. C refers to cubic cell with mirror (m) plane perpendicular to a twofold rotation axis. Parthe *et al.* [35] pointed on the impossibility of preparing RhS_2 phase that were previously reported by Juza *et al.* [33] as it led to a two-phase mixture containing elementary S and Rh_2S_3. These are as far to my knowledge, all the rhodium sulfide phases that have been characterized experimentally till date.

Out of all these three phases of rhodium sulfide Rh_2S_3, Rh_3S_4 and $Rh_{17}S_{15}$, Rh_2S_3 is an electronic insulator comprising of RhS_6 octahedra. Figure 1.3 shows the atomic arrangement of Rh_2S_3. In this crystal, six sulfur atoms (denoted by yellow) occupy the vertices of a distorted octahedron and surround one rhodium atom (denoted by blue). There is another S atom which is surrounded by four Rh atoms forming a distorted tetrahedron.

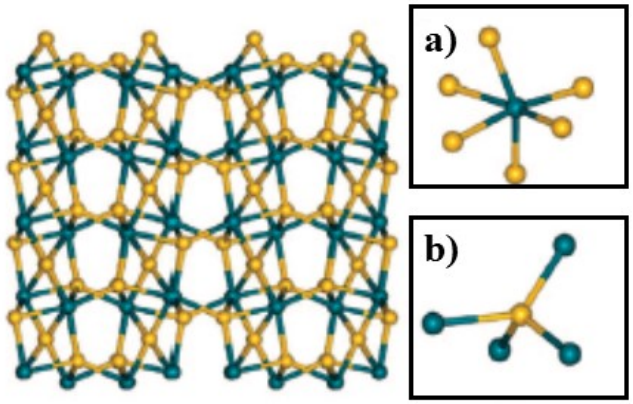

Fig. 1.3. 3-D crystal structure of Rh_2S_3 [37].
The inset show cluster of a) RhS_6 and b) Rh_4S. Blue and yellow spheres represent Rh and S atoms, respectively

The average Rh-Rh bond distance in Rh_2S_3 is 3.208 Å which is significantly larger than the Rh-Rh bond in pure Rh (2.731 Å) metal, thus removing any possibility of metallic Rh-Rh bond in the crystal. The whole crystal structure can be imagined as an alternating stacking sequence of octahedron pair layers along the (010) surface [38].

A representation of the monoclinic Rh_3S_4 cluster is shown in Figure 1.4, which has a complex unit cell with 42 atoms. Besides strands of edge sharing RhS_6 octahedara which are

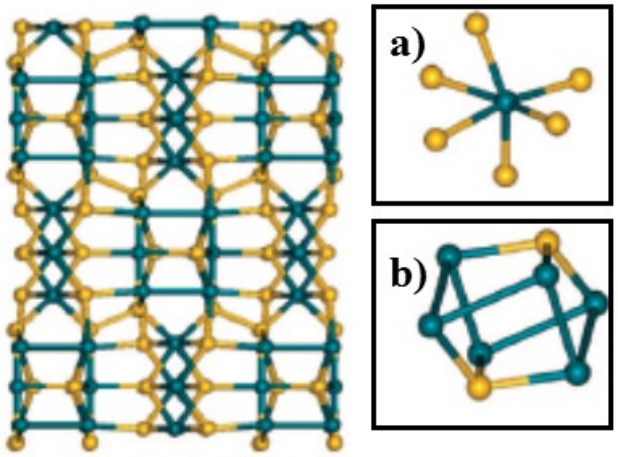

Fig. 1.4. 3-D crystal structure of Rh_3S_4 [37].
The inset show cluster of a) RhS_6 and b) Rh_6S_2. Blue and yellow spheres represent Rh and S atoms, respectively

connected by S-2 pairs (S-S=2.20 Å) [36], the crystal structure of Rh_3S_4 also contains Rh_6 clusters of Rh-Rh bond length of 2.731 Å. As Beck *et al.* [36] discovered, Rh_3S_4 has the composition in between the neighbouring phases of Rh_2S_3 and $Rh_{17}S_{15}$ as the structure contains RhS_6 octahedra which are found in Rh_2S_3 and domains of metal-metal bonds as found in $Rh_{17}S_{15}$. This Rh-Rh bond length is similar to the bond length in pure Rh, which characterizes Rh_3S_4 as a metallic conductor.

In contrast, the $Rh_{17}S_{15}$ phase consisting of Rh_8 octahedra with an average Rh-Rh distance of 2.59 Å possesses metallic properties [39] at room temperature, thus brings improved activity of $Rh_{17}S_{15}$ as the Rh-Rh bond is much stronger than the previous Rh_2S_3 and Rh_3S_4 phase.

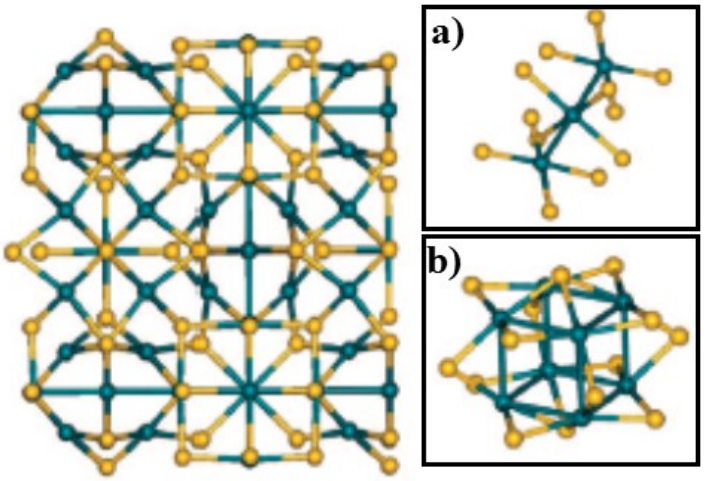

Fig. 1.5. 3-D crystal structure of $Rh_{17}S_{15}$ [37].
The inset show cluster of a) RhS_4 chains and b) sulfided Rh_8 cube. Blue and yellow spheres represent Rh and S atoms, respectively.

The primitive cubic $Rh_{17}S_{15}$ with $Pm\bar{3}m$ space group comprises of two unique Rh-S regions: cubes of Rh_8S_{14} and a series of RhS_4. Out of the four inequivalent Rh atoms, one Rh atom is surrounded by six S atoms forming a perfect octahedron and the other three Rh atoms have four S neighbours each as shown in Figure 1.5.a and 1.5.b respectively. Table 1.1 below summarizes the crystallographic properties of the different phases of rhodium sulfide.

Table 1.1. Crystallography of Rh_2S_3 [35], Rh_3S_4[36], $Rh_{17}S_{15}$ [35] and Rh (JCPDF #01-1214)

	Symmetry	Space group	Cell Parameters a (Å)	b (Å)	c (Å)	α (°)	β (°)	γ (°)	Rh-Rh_{avg} (Å)	Rh-S_{avg} (Å)
Rh_2S_3	ortho-rhombic	*Pbcn*	8.462	5.985	6.138	90	-	-	3.208	2.365
Rh_3S_4	monoclinic	*C2/m*	10.292	10.671	6.213	90	107.71	90	2.70/3.092	2.30
$Rh_{17}S_{15}$	cubic	$Pm\bar{3}m$	9.911	-	-	90	-	-	2.59	2.33
Rh	cubic	*Fm3m*	3.803	-	-	90	-	-	2.69	

1.5. Phase Transition and Phase Equilibrium of Rhodium Sulfide Compounds

The problem of phase stability and phase transition in solids has fascinated physicists, chemists, and material scientists for over a century, which still remains as one of the most challenging topics for material synthesis. In terms of applications, tuning the structure permits one to fabricate materials with tailored properties for maximum efficiency and output. Typically, this involves the knowledge to establish how various phases transform to one another and attain an equilibrium state. The relationship between different phases can be represented by property *phase diagrams*. Intriguingly, rhodium-sulfide compounds have the capacity to transform into different phases at high temperatures and achieve a phase equilibrium with reaction time.

In prior works [34-36], rhodium sulfide electro catalyst is shown to be a mixture of different crystalline phases with different valences and stoichiometry, in which it comprises of Rh_2S_3, Rh_3S_4, $Rh_{17}S_{15}$ and some amount of metallic rhodium. The potential route to synthesize different phases of rhodium sulfide is to control the sulfur content by application

of heat (thermal reduction) or by reacting Rh and S in required stoichiometric ratios as starting material in a sealed autoclave (hydrothermal reaction).

Recent studies made by Masud *et al.* [21], Ziegelbauer *et al.* [37] and Zhang *et al.* [31] concluded that the Rh_2S_3 is transformed into Rh_3S_4 and $Rh_{17}S_{15}$ and Rh metal by loss of sulfur during thermal treatment in inert gas atmosphere. Pure phase Rh metal exist above 850°C [21]. Sulfur content in the rhodium sulfide catalyst decreases with increasing reaction time by surface-to outside diffusion process until an equilibrium is reached between all the phases, which accordingly affects the phase composition at different temperatures and different reaction times. Figure 1.6 demonstrates the possible thermal reduction process of rhodium sulfide compounds.

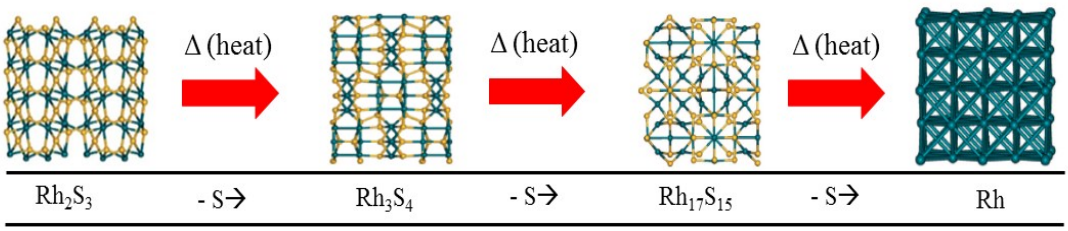

Fig. 1.6. Possible route of transition between different phases of rhodium sulfide Crystal structures Rh_2S_3, Rh_3S_4, $Rh_{17}S_{15}$ and Rh are taken from ref [37].

Dieguez *et al.* [38] and Jacob *et al*. [40] studied the thermodynamic properties of three phases of rhodium sulfide and found a very small gap between the energy of formation of Rh_2S_3, Rh_3S_4 and $Rh_{17}S_{15}$ *viz*. -4.83 eV/atom (Rh_2S_3), -5.05 eV/atom (Rh_3S_4) and -4.73 eV/atom ($Rh_{17}S_{15}$). 1 eV/atom is equal to 96.52 kJ/mol. Figure 1.7 shows the Gibb's free energy of formation published by Dieguez in 2009. This small gap of formation between the three phases indicate that the temperature gap between the formation of different Rh-S compounds is also small as Gibb's free energy is related to temperature. Hence, a temperature difference of 10°C was undertaken during our thermal reduction process.

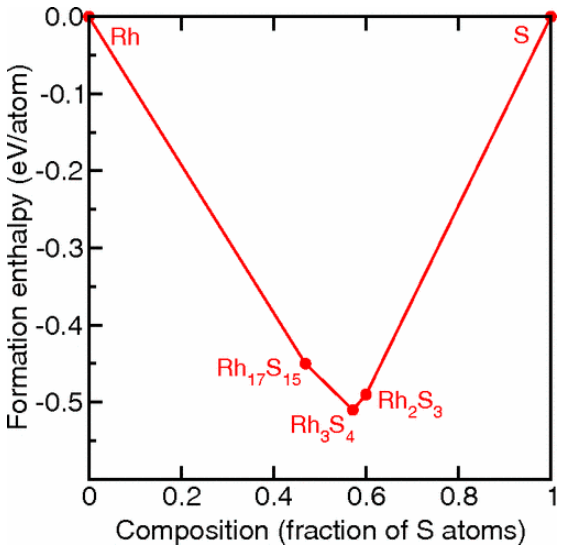

Fig. 1.7. Formation enthalpy of rhodium sulphide phases [38].

1.6. Objective of this work

Carbon supported rhodium sulfide catalyst is seen as a promising electrocatalyst for hydrogen bromine fuel cell as it is active as HER/HOR catalyst and is more stable than expensive Pt/C in the corrosive HBr/Br_2 electrolyte [15, 24] . The rhodium sulfide catalyst consists of several phases (Rh_2S_3, Rh_3S_4, $Rh_{17}S_{15}$) and Rh metal with Rh_2S_3 reported as true semiconductor [38] and Rh_3S_4, $Rh_{17}S_{15}$ being reported as conducting semi-metals [31, 36]. Therefore, an ideal catalyst for HOR/HER would be the one with minimum amounts of Rh metal (due to instability in HBr environment), Rh_2S_3 (due to their low activity) and a high concentration of Rh_3S_4 and $Rh_{17}S_{15}$.

In studying the effect of the constituent phases of rhodium sulfide electro catalyst on HOR/HER activity, it is paramount to understand and optimize the composition of rhodium sulfide phases by controlling the temperature and time of reaction under constant inert gas pressure. Since Rh_2S_3 is converted to the other phases by loss of sulfur, it would be of great interest to plot an equilibrium phase composition of rhodium sulfide at different

temperatures. This, I believe to my knowledge, will be the first reported equilibrium phase diagram of rhodium sulfide compounds supported on high surface area carbon.

The objective of this work is to synthesize rhodium sulfide catalyst and understand the relationship of the electrocatalytic activity to the phases present in the catalysts. An effort was made to provide an equilibrium phase diagram of rhodium sulfide catalyst from temperature range of 650°C to 700°C. By synthesizing carbon-supported rhodium sulfide electrodes with different phases at different temperatures, their contributions to the hydrogen oxidation and evolution was determined.

1.7. References

1. IEA. *2012 Key World Energy Statistics*. 4.13.15]; https://www.iea.org/publications/freepublications/publication/KeyWorld2014.pdf].
2. Yang, Z., et al., *Electrochemical Energy Storage for Green Grid.* Chemical Reviews, 2011. 111(5): p. 3577-3613.
3. Chen, H., et al., *Progress in electrical energy storage system: A critical review.* Progress in Natural Science, 2009. 19(3): p. 291-312.
4. Weber, A., et al., *Redox flow batteries: a review.* Journal of Applied Electrochemistry, 2011. 41(10): p. 1137-1164.
5. Nguyen T. V., S.R.F., *Flow Batteries.* The Electrochemical Society Interface, 2010(Fall): p. 54.
6. Thaller, L.H., *Electrically Rechargeable Redox Flow Cell*. US Patent 3996064. December 1976.
7. Thaller, L.H., *Redox Flow Cell Energy Storage Systems*. 1979, National Aeronautics and Space Administration, Lewis Research Center.
8. Remick, R.J. and P.G.P. Ang, *Ion selective membrane separate anolyte and catholyte*. US Patent 4485154. 1984.
9. Skyllas-Kazacos, M. and F. Grossmith, *Efficient Vanadium Redox Flow Cell.* Journal of The Electrochemical Society, 1987. 134(12): p. 2950-2953.
10. Skyllas-Kazacos, M., *Novel vanadium chloride/polyhalide redox flow battery.* Journal of Power Sources, 2003. 124(1): p. 299-302.
11. Cathro, K.J., K. Cedzynska, and D.C. Constable, *Preparation and performance of plastic-bonded-carbon bromine electrodes.* Journal of Power Sources, 1987. 19(4): p. 337-356.

12. Lopez-Atalaya, M., et al., *Optimization studies on a Fe/Cr redox flow battery.* Journal of Power Sources, 1992. 39(2): p. 147-154.

13. Livshits, V., A. Ulus, and E. Peled, *High-power H2/Br2 fuel cell.* Electrochemistry Communications, 2006. 8(8): p. 1358-1362.

14. Kreutzer, H., V. Yarlagadda, and T. Van Nguyen, *Performance Evaluation of a Regenerative Hydrogen-Bromine Fuel Cell.* Journal of The Electrochemical Society, 2012. 159(7): p. F331-F337.

15. Nguyen, T.V., et al., *HER/HOR Catalysts for the H2-Br2 Fuel Cell System.* ECS Transactions, 2013. 53(7): p. 75-81.

16. Yeo, R.S. and D.T. Chin, *A Hydrogen-Bromine Cell for Energy Storage Applications.* Journal of The Electrochemical Society, 1980. 127(3): p. 549-555.

17. Werner, G. and B. G. H, *Performance of Hydrogen-Bromine Fuel Cells*, in *Fuel Cell Systems*. 1969, AMERICAN CHEMICAL SOCIETY. p. 203-220.

18. Baldwin, R.S., *Electrochemical performance and transport properties of a Nafion membrane in a hydrogen-bromine cell environment*. 1987, NASA Lewis Research Center; Cleveland, OH, United States.

19. Cho, K.T., et al., *High Performance Hydrogen/Bromine Redox Flow Battery for Grid-Scale Energy Storage.* Journal of The Electrochemical Society, 2012. 159(11): p. A1806-A1815.

20. Goor-Dar, M., N. Travitsky, and E. Peled, *Study of hydrogen redox reactions on platinum nanoparticles in concentrated HBr solutions.* Journal of Power Sources, 2012. 197(0): p. 111-115.

21. Masud, J., et al., *A RhxSy/C Catalyst for the Hydrogen Oxidation and Hydrogen Evolution Reactions in HBr.* Journal of The Electrochemical Society, 2015. 162(4): p. F455-F462.

22. Xiong, L. and A. Manthiram, *Effect of Atomic Ordering on the Catalytic Activity of Carbon Supported PtM (M = Fe , Co, Ni, and Cu) Alloys for Oxygen Reduction in PEMFCs.* Journal of The Electrochemical Society, 2005. 152(4): p. A697-A703.

23. Zhang, J., et al., *Stabilization of Platinum Oxygen-Reduction Electrocatalysts Using Gold Clusters.* Science, 2007. 315(5809): p. 220-222.

24. Ivanovskaya, A., et al., *Transition Metal Sulfide Hydrogen Evolution Catalysts for Hydrobromic Acid Electrolysis.* Langmuir, 2013. 29(1): p. 480-492.

25. Allen, R.J., Giallombardo, J.R., Czerwiec, D., Castro, E.D., Shaikh, K., *Rhodium electrocatalyst and method of preparation*. US Patent 6149782. 2000.

26. Lee, J., et al., *Novel hydrodesulfurization catalysts derived from a rhodium carbonyl complex.* Journal of Molecular Catalysis A: Chemical, 2004. 209(1–2): p. 155-162.

27. Gullá, A.F., et al., *Carbon-supported low-loading rhodium sulfide electrocatalysts for oxygen depolarized cathode applications.* Applied Catalysis A: General, 2007. 326(2): p. 227-235.

28. Ziegelbauer, J.M., et al., *Chalcogenide electrocatalysts for oxygen-depolarized aqueous hydrochloric acid electrolysis.* Electrochimica Acta, 2007. 52(21): p. 6282-6294.

29. Tsou, Y., Deng, H., Martelli, G.N., Allen, R. J., Castro, E.S.D., *Rhodium electrocatalyst and method of preparation*. US Patent 6855660. 2002.

30. Solorza-Feria, O., et al., *Novel low-temperature synthesis of semiconducting transition metal chalcogenide electrocatalyst for multielectron charge transfer: molecular oxygen reduction.* Electrochimica Acta, 1994. 39(11–12): p. 1647-1653.

31. Zhang, W., et al., *Phase Controllable Synthesis of Well-Crystallized Rhodium Sulfides by the Hydrothermal Method.* Crystal Growth & Design, 2009. 9(8): p. 3765-3770.

32. Allen, R.J. and A.F. Gulla, *Synthesis of noble metal, sulphide catalysts in a sulfide ion-free aqueous environment*. US Patent 6967185, 2005.

33. Juza R, H.O., Meisel K, Biltz W, *Studies of alkali-aluminium silicates.* Journal of Inorganic Chemistry, 1935. 225: p. 369.

34. Geller, S., *The crystal structure of the superconductor Rh17S15.* Acta Crystallographica, 1962. 15(12): p. 1198-1201.

35. Parthé, E., E. Hohnke, and F. Hulliger, *A new structure type with octahedron pairs for Rh2S3, Rh2Se3 and Ir2S3*. Acta Crystallographica, 1967. 23(5): p. 832-840.

36. Beck, J. and T. Hilbert, *Ein ‚altes' Rhodiumsulfid mit überraschender Struktur: Synthese, Kristallstruktur und elektronische Eigenschaften von Rh3S4*. Zeitschrift für anorganische und allgemeine Chemie, 2000. 626(1): p. 72-79.

37. Ziegelbauer, J.M., et al., *Fundamental Investigation of Oxygen Reduction Reaction on Rhodium Sulfide-Based Chalcogenides.* The Journal of Physical Chemistry C, 2009. 113(17): p. 6955-6968.

38. Diéguez, O.M., Nicola, *First-principles characterization of the structure and electronic structure of α-S and Rh-S chalcogenides.* Physical Review B, 2009. 80(21).

39. Li, Y., et al., *Spherical Rh17S15@C and Rh@C core–shell nanocomposites: Synthesis, growth mechanism and methanol tolerance in oxygen reduction reaction.* Chemical Engineering Journal, 2013. 228(0): p. 45-53.

40. Jacob, K.T. and P. Gupta, *Gibbs free energy of formation of rhodium sulfides.* The Journal of Chemical Thermodynamics, 2014. 70(0): p. 39-45.

CHAPTER 2
EXPERIMENTAL AND COMPUTATIONAL STUDIES

In this chapter, we first provide the method to synthesize rhodium sulfide precursor supported on high surface area carbon (C) as described in the patent literature [1]. Next, the process of thermal reduction to make active phases of rhodium sulfide in a quartz-tube furnace is discussed. Electrode preparation and electrochemical measurement setups are provided and the last section provides an understanding to the approach for efficiently finding the quantitative phase composition using Rietveld refinement in GSAS-II software.

2.1. RHODIUM SULFIDE ON CARBON SUPPORT CATALYST SYNTHESIS

Noble metal chalcogenides are extensively used in electrocatalysis; particularly for rhodium and ruthenium sulfide for use as oxygen reduction cathodes in the electrolysis of hydrochloric acid [2-4]. Prior to the invention of the hydrogen sulfide free (HSF) synthesis, noble metal sulfides were prepared by purging hydrogen sulfide gas through an aqueous solution of corresponding noble metal precursor [5], but this process ran into safety and health issues associated with the handling of flammable and noxious H_2S gas. So, an alternative synthesis route for production of noble metal sulfides by eliminating the use of H_2S gas was proposed by Allen *et al.* in 2005. A flowchart of the HSF synthesis process is shown in Figure 2.1.

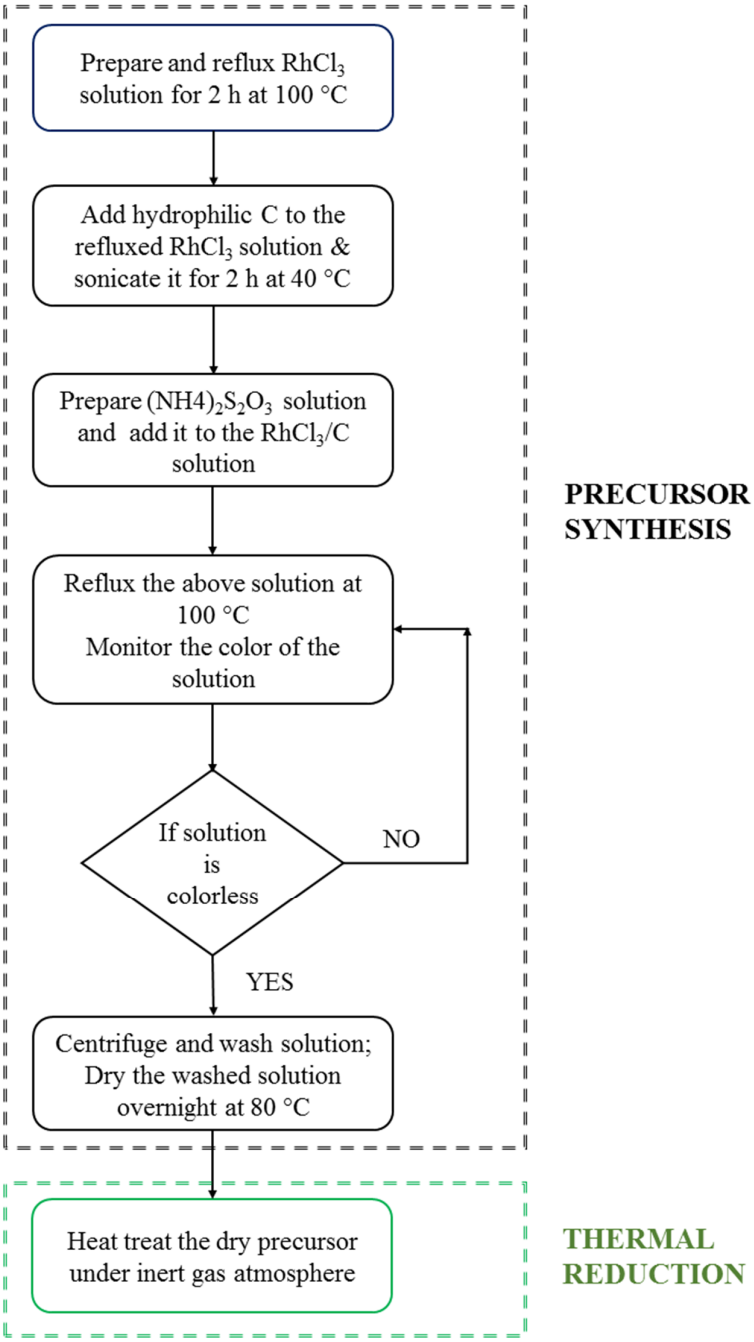

Fig. 2.1. Flowchart of hydrogen sulfide free catalyst synthesis

2.1.1. Precursor Synthesis

Rhodium (III) chloride hydrate ($RhCl_3.3H_20$) (Alfa Aesar) was dissolved in deionized (DI) water in the ratio ($RhCl_3.3H_20$:DI water=7.62 g:1 L) and the solution was

refluxed in a round bottom flask (RBF) for 2 h to ensure the dissociation of rhodium (Rh^{3+}) and chloride (Cl^-) ions and to remove any volatile impurities. After reflux, the solution was cooled down to room temperature (RT).

High surface area Vulcan XC-72R carbon (C) powder (Cabot Cooperation) which has a specific surface area around 250 m^2/g and is formed by an aggregation of 30-60 nm size-particles was used as carbon support for the rhodium sulfide catalyst. The carbon powder was pre-treated initially to remove any moisture by heat treating at 100°C in Argon (Ar) atmosphere for 30 min. Vulcan XC-72R. The heat-treated C powder was then allowed to cool to room temperature (RT) under Ar flow and then stored in a sealed vial. A calculated amount of this pre-treated C powder was weighed in the ratio Rh:C=1:3 (wt %) and the hydrophobic C powder was made hydrophilic by boiling in DI water at 100°C for 30 min. This conversion from hydrophobic to hydrophilic carbon is important because hydrophilic carbon will ensure the uniform distribution of rhodium ions on the carbon powder in the subsequent step. No effort was made to analyse the functional groups on the surface of the carbon. The carbon solution was allowed to cool down to RT. Figure 2.2 shows a) hydrophobic C and b) hydrophilic C after heat treating in DI water.

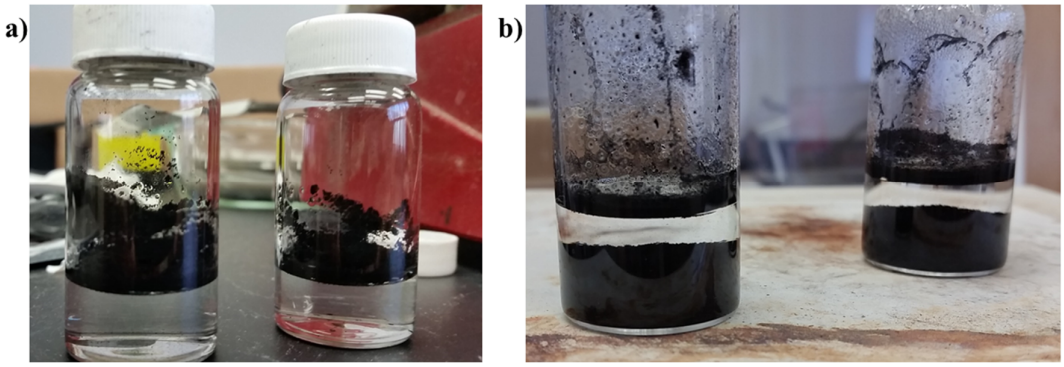

Fig. 2.2. Vulcan XC-72R carbon a) before and b) after heat-treating in DI water

The hydrophilic C was then transferred to the refluxed $RhCl_3$ solution and sonicated for 2 h at 40°C in a SRA Ultrasonic cleaner (Model UC-20D) at a frequency of 40 kHz to prepare a uniformly dispersed rhodium/Vulcan solution. Meanwhile, ammonium thio-sulfate ($(NH_4)_2S_2O_3$) solution was prepared by mixing ($(NH_4)_2S_2O_3$) (Alfa Aesar) crystals in the molar ratio (Rh:S=2:3) and DI water in the ratio (($(NH_4)_2S_2O_3$):DI water=8.64 gm: 60 ml).

After sonication, the rhodium/Vulcan solution was transferred to a reflux column and heated to 70°C while stirring continuously with a magnetic stirrer. Once the solution temperature reaches 70°C, the thiosulfate solution was added in three equivalent aliquots, one in every 2 minutes. After the last aliquot was added, the resulting solution was refluxed at 100°C. The reaction was monitored by constantly checking the color changes from initial deep pink/orange color (due to the presence of free Rh^{3+} ions), which progressively turned colorless upon completion of the reaction. This was done by pipetting out a small aliquot of the refluxed solution from the RBF and centrifuging it for 5 min. Centrifuging was done at 3400 rpm in a Cole-Parmer Centrifuge (Model No: 17250-10). The color of the solution collected after centrifuging was observed and the RBF was cooled down to RT if the solution was colorless indicating completion of reaction. The completion of the reaction may take 1 h to 3 h, depending on the amount of selected precursor and the reaction conditions. Figure 2.3 shows a) deep pink color/orange color and b) colorless solution after centrifuging.

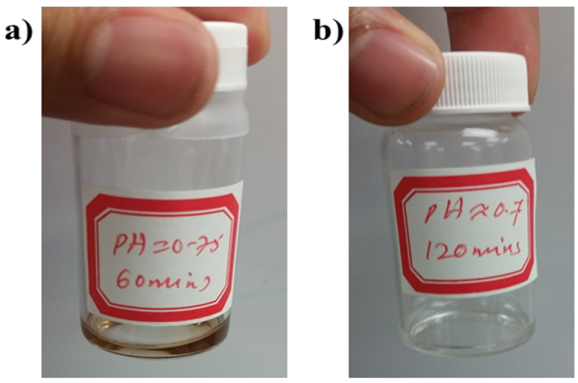

Fig. 2.3. a) Deep pink/orange color and b) colorless solution obtained after centrifuging

The reactions undergoing during the HFS process are as follows,

a) Dissociation of $RhCl_3(H_2O)_3$ to Rh^{3+} and Cl^- ions during refluxing at 100°C:

$$RhCl_3(H_2O)_3 \rightarrow 3H_2O + Rh^{3+} + 3Cl^-$$

b) Ammonium thio-sulfate solution undergoes disproportionation reaction, giving sulfide (S^2) ions and sulphuric acid:

$$(NH_4)_2S_2O_3 \rightarrow 2NH_4^+ + S_2O_3^{2-}$$

$$3S_2O_3^{2-} + 3H_2O \rightarrow 3S^{2-} + 3H_2SO_4$$

c) Once the ammonium thio-sulfate solution is added to the rhodium/Vulcan solution, three S^{2-} ions react with two Rh^{3+} ions to form rhodium sulfide (Rh_2S_3) and NH_4^+ ions react with Cl^- ions to form water soluble NH_4Cl at temperatures between 50°C and 100°C,

$$2Rh^{3+} + 3S^{2-} + 6NH_4^+ + 6Cl^- \rightarrow 6NH_4Cl + Rh_2S_3$$

After the completion of the reaction *i.e.* when all the Rh^{3+} ions were converted to Rh_2S_3, the solution was cooled down to RT. The final solution was then collected in 50 ml centrifuge tubes and were centrifuged for 5 min for about 4-5 times. Every wash, the centrifugate was replaced with DI water. The precipitate after final washing was collected in petri dishes, covered with Kimwipe paper and air-dried at 80°C overnight. The dried product was finally grinded in a mortle and pestle and stored in sealed vials. The grinded dried product or precursor is a semiconductor and is amorphous in nature [6].

2.1.2. Thermal Reduction

The powdered catalyst was then placed in a sample holder shown in Figure 2.4.c and heat treated in a quartz tube furnace under flowing ultra-high purity Ar (Matheson) as shown in Figure 2.4.b. A schematic figure of the setup of the thermal treatment of the catalyst is shown in Figure 2.4.a. The inner diameter (ID) and outer diameter (OD) of the quartz tube were 5 cm and 4.6 cm respectively. The thermal reduction was executed under Ar flowrate of

148 cc/min (2 bubbles per second) to prevent any oxide formation from RT to 650°C, 660°C, 670°C, 680°C, 690°C and 700°C and all catalysts were heated at the final temperature for 3 h. The reason for considering higher reaction time (180 min) as compared to the reaction time of 30 min reported by Masud *et al.* [6] was to attain an equilibrium phase composition which is discussed in Section 3.1. Previous X-ray photoelectron spectroscopy (XPS) study [6] done by Dr. Nguyen's group on the synthesized catalysts observed the formation of functional group on the carbon surface but no rhodium oxide or rhodium carbide formation was observed.

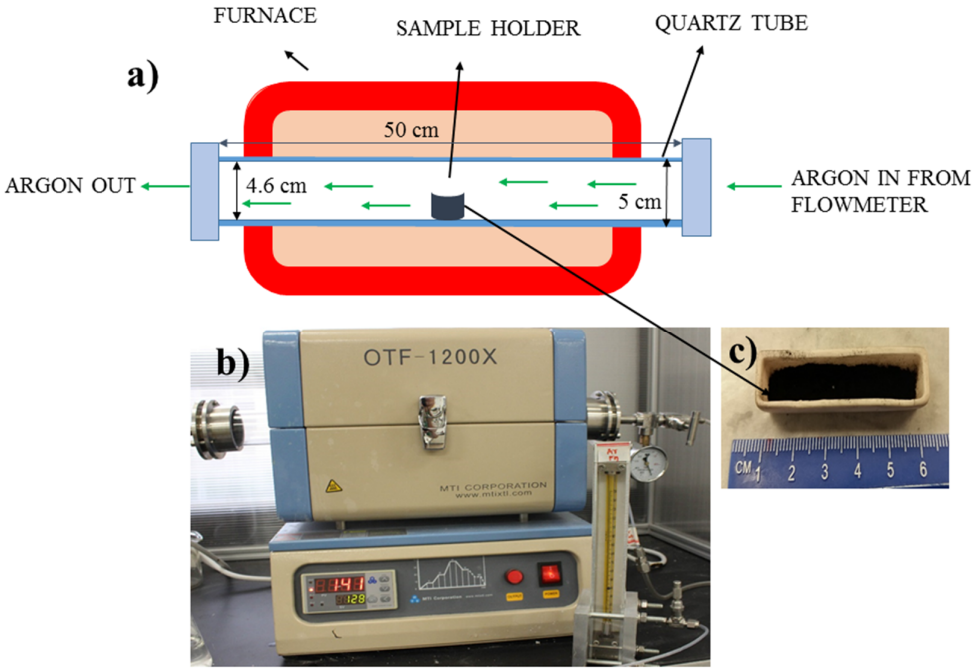

Fig. 2.4. a) Schematic of quartz-tube furnace b) Quartz-tube furnace set-up and c) sample holder with catalyst sample

The ramp rates as reported in the literature [6] were set in the furnace during the thermal reduction,

For 650°C: RT to 600°C at 10°C/min (ramp rate 1); 600°C to 625°C at 2°C/min (ramp rate 2); and 625°C to 650°C at 1°C/min (ramp rate 3);

For 660°C: RT to 610°C at 10°C/min; 610°C to 635°C at 2°C/min and 635°C to 660°C at 1°C/min.

For 670°C: RT to 620°C at 10°C/min; 620°C to 645°C at 2°C/min and 645°C to 670°C at 1°C/min.

For 680°C: RT to 630°C at 10°C/min; 630°C to 655°C at 2°C/min and 655°C to 680°C at 1°C/min.

For 690°C: RT to 640°C at 10°C/min; 640°C to 665°C at 2°C/min and 665°C to 690°C at 1°C/min.

For 700°C: RT to 650°C at 10°C/min; 650°C to 675°C at 2°C/min and 675°C to 700°C at 1°C/min.

To monitor the temperature inside the furnace, a calibration was performed using a K-type thermocouple by purging Ar gas at 148 cc/min and heating the furnace to 650°C with the above mentioned ramp rates *i.e.* ramp rate 1 (RT to 600°C at 10°C/min), ramp rate 2 (600°C to 625 C at 2°C/min), ramp rate 3 (625°C to 650°C at 1°C/min), final T set for 60 min and then allowed to cool down without disturbing the setup. Using Omega Engineering data acquisition system (DAS) (Model: OMB-DAQ-54), the temperature was recorded every 1 min and the graph 'T vs t' is shown in Figure 2.5. No optimization of the ramp-rates was performed to see the effect of composition changes.

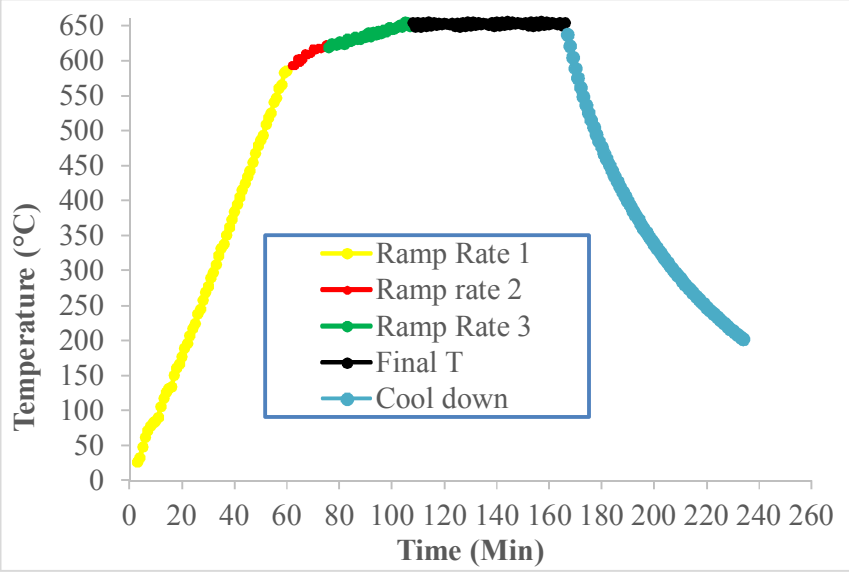

Fig. 2.5. Temperature (T) vs time (t) plot at different ramp rates during thermal reduction

a)

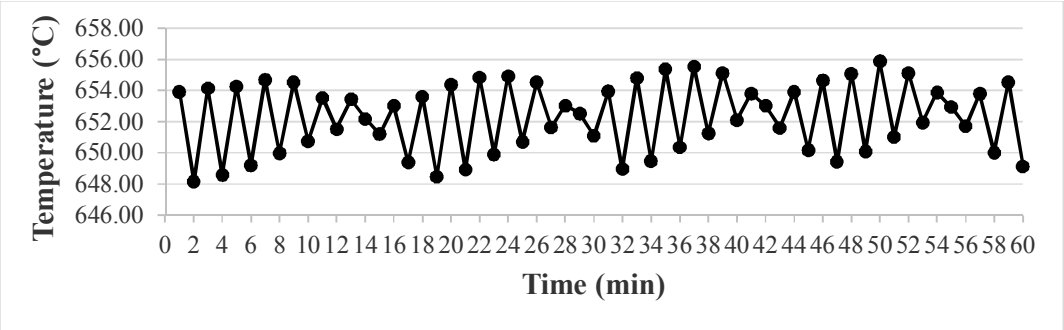

b).

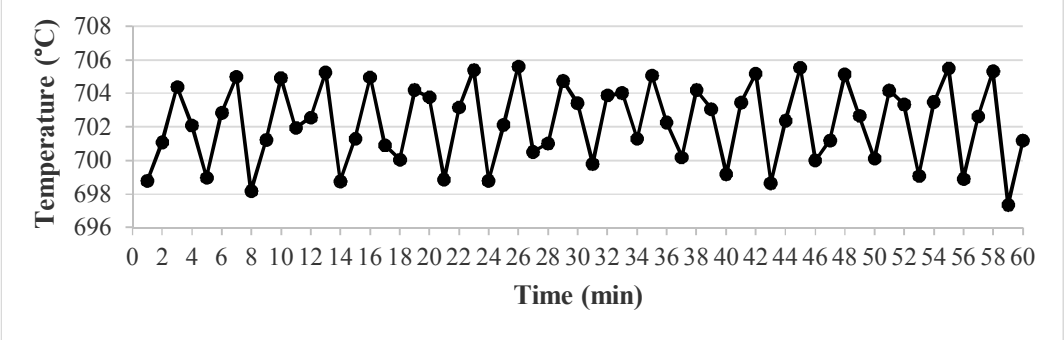

Fig. 2.6. Plot showing the variation of temperature (T) with time (t) when the temperature in the quartz-tube furnace was set for a) 650°C and b) 700°C

The variation of T inside the furnace was significant at the final temperature of 650°C as shown in Figure 2.6.a. The actual temperature when the furnace was set for 650°C, varied from 652±4°C. Similarly, purging Ar at 148 cc/min, the temperature was recorded inside the furnace using the K-type thermocouple when the temperature was set for 700°C as shown in Figure 2.6.b. The variation observed in T at final T of 700°C was almost similar (702±4°C) to the final T of 650°C. From the above observation, as I used the same ramp rates for each temperature, I summarized an approximate relative temperature range inside the furnace at different final set T during the thermal reduction process. But, to refer the different final T, I will be using the standard notation instead of the T range in the rest of the thesis.

Table 2.1. Actual T range inside the furnace versus the final set T inside the quartz-tube furnace

Temperature set (°C)	650	660	670	680	690	700
Actual T (°C) inside the furnace	652±4	662±4	672±4	682±4	692±4	702±4

2.2. EXPERIMENTAL PROCEDURE

2.2.1. Catalyst Ink Preparation

Even though a lot of research has been done in the field of catalyst ink preparation to improve the catalyst utilization by optimizing Nafion and Teflon content in the catalyst ink [7, 8], the protocol developed by Nguyen's group [6] was followed for preparing the rhodium sulfide on carbon support (Rh_xS_y/C) catalyst ink in this project, because of the possible repulsive nature of Nafion towards sulfides.

For the catalyst ink preparation, Rh_xS_y/C heat treated at different temperatures (650°C-700°C) were used as catalyst material. Further, Liquion^{TM} Nafion 15 wt % 1000 EW solution from Ion Power Inc. was diluted with 50:50 wt % IPA: DI water solution to make 0.1 wt % Nafion solution. A weighing balance of model no. GH-202 (accuracy 0.01 mg) by A&D Company was used.

The steps to prepare the catalyst ink were as follows,

1) Add 2 mg Rh_xS_y/C in a dry glass vial.

2) Add 60 µl of DI water to wet the catalyst in order to prevent it from burning when isopropyl alcohol (IPA) is added in step 3.

3) Add 1 ml IPA to the above solution.

4) Seal the vial with wax paper and transfer it to a water bath.

5) Sonicate the dispersion for 30 min.

2.2.2. Electrode Preparation

Glassy carbon rotating disk electrode (GC-RDE) of 5 mm diameter from Pine Instruments was polished to a mirror finish with 0.05 µm alumina suspensions (Allied High Tech Products, Inc) before each electrochemical experiment. A quantity of 30 µl of the catalyst ink was pipetted out with a micro syringe (Hamilton, Model Model 710 N SYR) and added drop wise on the surface of the GC RDE. Between each drop, the ink was allowed to dry under a table-lamp. The catalyst layer was then allowed to dry at 80°C for 15 min to remove any excess moisture. After drying, an aliquot of 10 µl 0.1 wt % Nafion solution was dropped over the catalyst layer. The Nafion-coated working electrode was initially dried at room temperature and then finally heated to 80°C for 30 min in an oven.

The amount of catalyst loaded in the GC-RDE is crucial for calculation of mass-specific electrochemical active surface area (ESCA) (cm^2/mg of catalyst). Since the amount of catalyst used in the GC-RDE was too less to measure accurately, a different method was used to determine the catalyst loading in the GC-RDE by dispersing the catalyst ink in carbon paper. For this, a piece of SGL 10 AA carbon paper of roughly 1 cm^2 area was air-dried and weighed. A 30 µl of catalyst ink was then dropped into the dry carbon paper and was then air-dried at 80°C for 1 h in an oven. The weight of the catalyst coated is the difference between the initial weight of the dry carbon paper and its weight after coating and drying the ink. To ensure reproducibility, three readings were taken for each sample in the micro-balance whose accuracy is 0.01 mg. The final catalyst (Rh_xS_y/C) loading of all the studied catalysts varied from 0.06-0.07 mg.

2.2.3. RDE Experimental Setup

Rotating Disk Electrode (RDE) measurements were performed in a conventional three-electrode electrochemical cell at RT with a Gamry (G300) Potentiostat/Galvanostat. As shown in Figure 2.7.

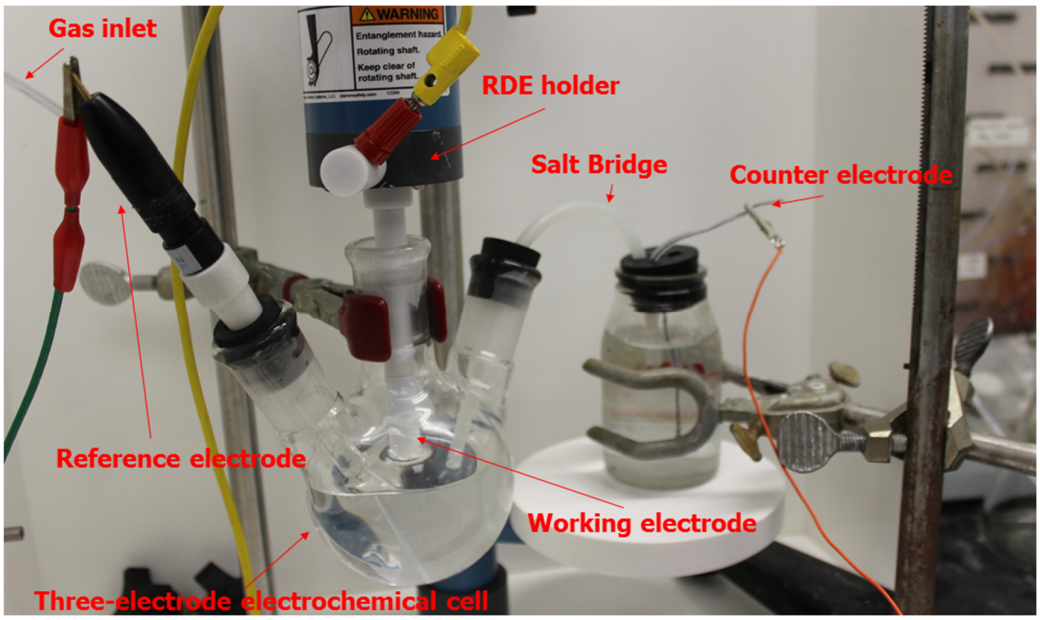

Fig. 2.7. RDE experimental set-up

The GC-RDE coated with catalyst-Nafion layer acts as the working electrode and a saturated calomel electrode (SCE) was taken as the reference electrode. A piece of Platinum (Pt) foil of area 1 cm^2 served as the counter electrode which was placed in a separate chamber and connected to the three-electrode electrochemical cell *via* a KCl salt-bridge. The electrolyte, 1 M sulphuric acid (H_2S0_4) was prepared from certified ACS Plus grade H_2SO_4 (Fischer Scientific) by diluting with DI water. The electrolyte was deaerated within the cell at least 15 min prior to the immersion of the working electrode. The rotation rate of RDE was controlled by a Pine Instrument Analytical Rotator with maximum speed of 2500 rpm. Before each electrochemical measurements, the working electrode was soaked in DI water for 1 h to ensure that the Nafion binder is well hydrated. Fresh electrolyte was used for each electrochemical measurement. All the potentials reported herein are with respect to the reversible hydrogen electrode (RHE) potential. All measurements were operated at RT and to prevent H_2 bubble accumulation over the catalyst layer surface, the RDE holder was tilted to about 10 degrees.

2.2.4. Cyclic Voltammetry (CV) in 1 M H_2SO_4

It is well known that electric current of an electrochemical process is proportional to the real surface area of an electrode. The real surface area can be evaluated by determining the atoms or molecules that adsorb onto the catalyst surface. Since every adsorbed atom is attached to an active site of the catalyst surface, by calculating the charge (Q_H) associated with the surface atoms and comparing it to charge density (Q_s) of a theoretically flat metal surface, one can determine the real surface area or electrochemical active surface area (ECSA) of the catalyst surface [9] *viz.* ECSA= Q_H/Q_s. Cyclic voltammetry (CV) is typically used to evaluate the ECSA of any catalyst.

In a standard CV measurement, the potential (V) applied to a working electrode is swept back and forth between two voltage limits while the response of the current (I) is measured. In my ECSA experiment, I have considered the charge under the voltammetric peak for desorption (shaded region in Figure 2.7), corrected for double layer charging current (I_{dl}), and assumed it to correspond to oxidation of one hydrogen atom on each reactive site on the Rh_xS_Y/C catalyst surface.

The solution of 1 M H_2SO_4 was initially deaerated with high-purity nitrogen (N_2) gas for nearly 30 min before starting the CV. The electrode surface was initially cleaned and activated by carrying out CV at a scan rate of 20 mV/s from 0 V to 0.925 V vs RHE (ca. 5 cycles) in N_2-purged electrolyte. This was followed by a CV from 0 V to 0.425 V vs RHE at a scan rate of 10 mV/s to avoid the oxidation of the materials at higher potentials that is known to lead to inconsistent ECSA measurements [6]. The CV was carried out until reproducible voltammograms were obtained (ca. 5 cycles). Figure 2.7 shows a typical CV plot for the hydrogen oxidation and reduction (HOR/HER) region of Rh_xS_y/C catalyst in an RDE in N_2 saturated 1 M H_2S0_4.

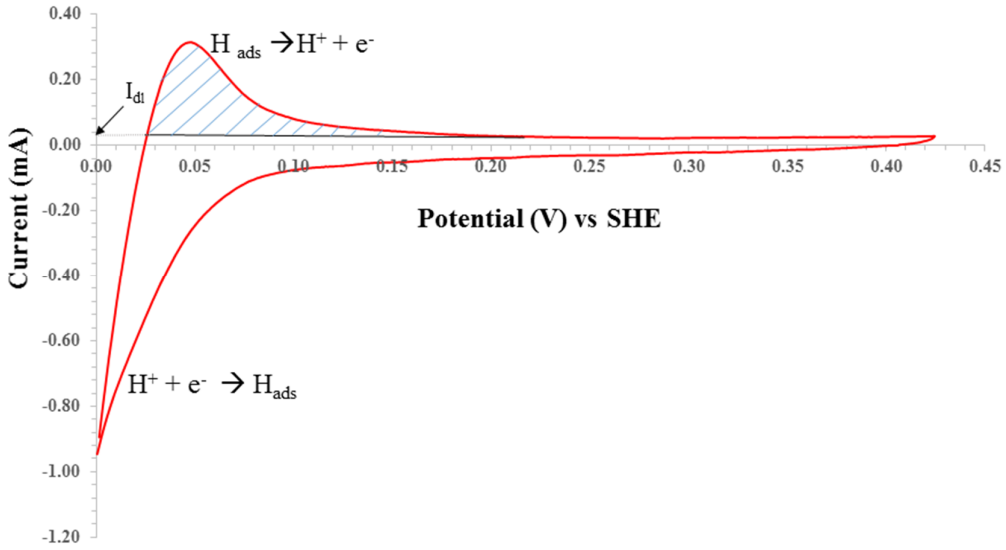

Fig. 2.8. Cyclic voltammogram of Rh_xS_y/C electrode in 1 M H_2SO_4 highlighting the region of interest. The shaded area is the charge due to H_{ads} oxidation during the forward scan and is used in the ECSA calculation

As mentioned, the charge (Q_H) obtained by integration of the hydrogen oxidation peak that resulted due to the forward scan was used to calculate the ECSA of our Rh_xS_y/C electrocatalyst,

$$ECSA\ (cm^2) = \frac{Q_H(\mu C)}{210\ (\frac{\mu C}{cm^2})}$$

where,

210 $\frac{\mu C}{cm^2}$ is the charge associated with the monolayer adsorption of hydrogen on Pt or Rh [10]. The ECSA in this thesis is reported by normalizing with the metal loading (mg of Rh).

2.2.5. Activity Measurement in 1 M H_2SO_4

The exchange current density, i_o of an electrochemical system is analogous to the rate constant in a chemical system. RDE measurement is a convenient approach for quantitative evaluation of electrocatalytic activity or exchange current density of high surface area electrocatalyst. It involves hydrodynamic principles, where the working electrode is rotated

to induce forced convection. In this thesis, HOR-HER activity measurements were conducted with the catalyst coated GC-RDE mounted onto an interchangeable RDE holder (Pine Instruments) in H_2-saturated 1 M H_2SO_4 solution.

The electrode multi-step chronoamperometry (MSCA) was performed to obtain the current versus potential (corrected for ohmic loss to obtain only kinetic parameters) curves in both the oxidation and reduction reactions. The RDE was rotated at 2000 rpm during the MSCA run. Polarization curves were obtained from open circuit potential (OCV) to ±0.020 V at a potential step of 0.002 V after obtaining a constant OCV of 0.0 ± .0001 V vs RHE. Each potential was held for 10 s to attain a steady value of the current and the average value of the last 3 points of current observed for each potential step was calculated and plotted versus overpotential (η) as shown in Figure 2.9.b. Furthermore, only the data in the kinetically controlled region or the linear region in the overpotential versus current plot (shown in the green circle in Figure 2.9) were used to calculate the catalyst activity. Electrochemical impedance spectroscopy (EIS) (Gamry EIS 300, Amplitude: 5mV and Frequency range: 0.1Hz to 100 kHz) was performed to obtain the ohmic loss (iR) between the working and reference electrodes.

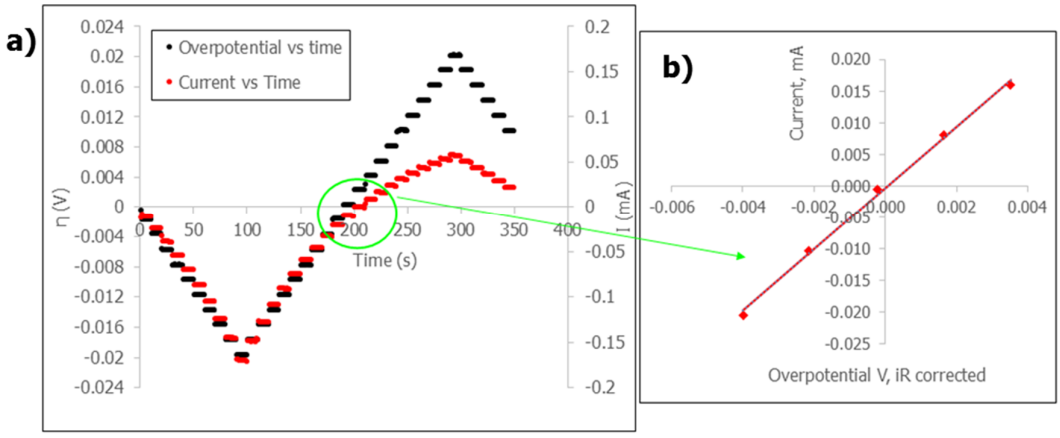

Fig. 2.9. a) Overpotential (η) versus time plot (black) and current versus time plot (red) as obtained from MSCA experiment (b) the linear region or kinetically controlled region used to

The exchange current density (current normalized to active area) of HOR/HER reactions was calculated using widely applied linearized Butler-Volmer approach [11],

$$i \cong a i_o \left\{ (a_a + a_c)(\frac{F}{RT}\eta) \right\}$$

where,

i= current density in Ampere (A) per cm^2 of geometric area

i_0= exchange current density in A per cm^2 of active area

a= active area / geometrical area

a_a = anodic transfer coefficients

a_c = cathodic transfer coefficients

F= Faraday's constant (96487 C/mol)

R= universal gas constant (8.314 J/mol.K)

T= operating temperature (K)

$\eta = \mathrm{E} - \mathrm{E_{eq}}$ = overpotential (-25 mV $\leq \eta \leq 25$ mV)

2.3. X- RAY DIFFRACTION AND RIETVELD ANALYSIS

2.3.1. Introduction to X-Ray Diffraction

X-Ray Diffraction (XRD) is a powerful technique to study crystal structures and for phase quantification of multiphase crystalline materials. X-rays, which are of order ~.01 nm to ~1 nm, scatters from atoms (~0.1 nm) resulting in spots giving unique diffraction patterns, which contains information about the atomic arrangement within the crystal.

Let us consider X-ray beams (1 and 2) of wavelength (λ) incident at an angle θ on a pair of parallel planes of atoms P1 and P2, separated by inter-planar distance (d) as shown in Fig 2.7.

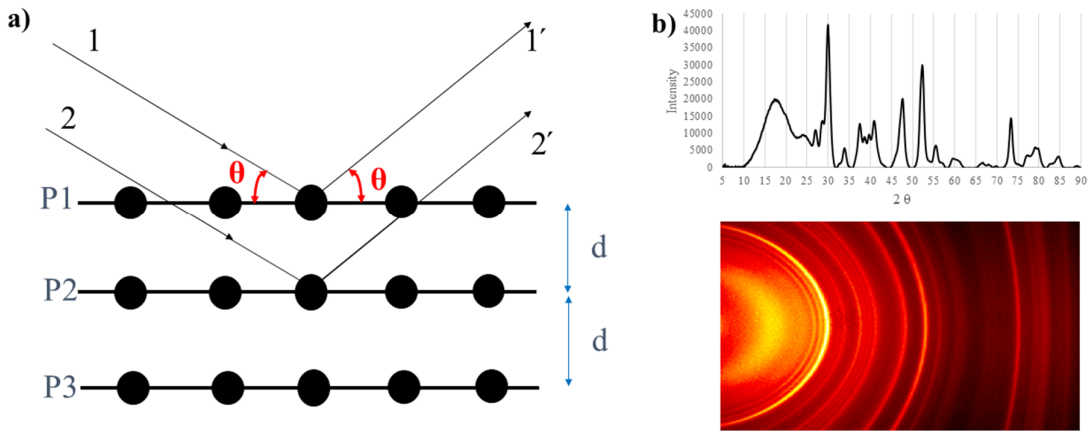

Fig. 2.10. (a) Diffraction of X-rays from planes of a crystal lattice (b) A typical diffraction pattern

A reflected beam of maximum intensity will occur only if the waves represented by 1′ and 2′ are in phase (constructive interference) and will be of minimum intensity if they are out of phase (destructive interference). The difference in path length between 1 to 1′ and 2 to 2′ must be then an integral number (n) of λ for constructive interference. This relationship, known as Bragg's law was discovered by Sir William H Bragg and Sir W. Lawrence Bragg in 1912,

$$2dsin\theta = n\lambda$$

where,

θ= scattering angle

n= integer

d= inter-planar distance (nm), and

λ= wavelength of incident ray (nm)

By varying the angle θ, the Bragg's law is satisfied by different d-spacing in polycrystalline materials. Plotting the angular positions and its reflected intensities produces

an X-Ray diffraction pattern as shown in Figure 2.7.b which is the fingerprint of a crystalline substance. Till date, there are more than 50,000 inorganic and 25,000 organic single components, crystalline phases, diffraction patterns discovered and collected as standard database [12].

2.3.2. Phase Identification of Crystal Structure

As each crystal structure generates a unique finger print in the form of diffraction pattern, the crystalline phases co-existing in a multiphase crystal can be identified by pattern matching with a standard diffraction data *via* modern-search match software. For this, we require standard diffraction patterns of crystalline substances. The International Centre of Diffraction Data (ICDD), formerly known as Joint Committee on Powder Diffraction Standards (JCPDS), is an organization that maintains the database of inorganic and organic substances. The database, known as Powder Diffraction File (PDF) database can be downloaded directly from ICDD website or is available from diffraction equipment manufacturer software. Finger print of Rh_2S_3 (ICDD No: 15344), Rh_3S_4 (ICDD No: 410813) and $Rh_{17}S_{15}$ (ICDD No: 410838) phases are shown in Figure 2.9.

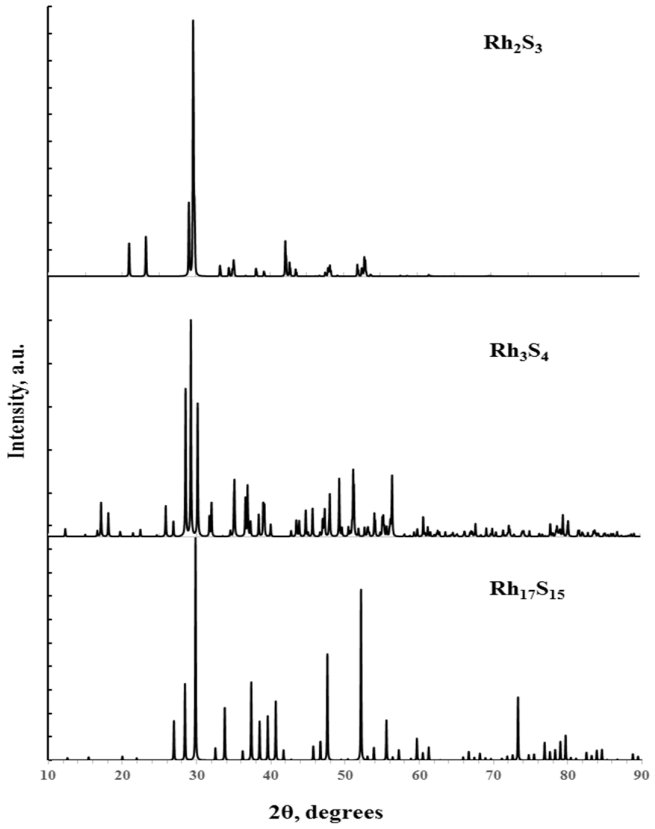

Fig. 2.11. Fingerprint region of Rh_2S_3 (ICDD No: 15344), Rh_3S_4 (ICDD No: 410813) and $Rh_{17}S_{15}$ (ICDD No: 410838)

2.3.3. Phase Quantification of Multiphase Crystal using Rietveld Analysis

Quantitative analysis of phases in a multiphase crystal by diffraction is based on the fact that the intensity of diffraction pattern of a particular phase in a mixture of phases is proportional to the concentration of that particular phase in that mixture. The first quantitative phase analysis using X-Ray Diffraction was done by Clark *et al.* in 1936 [13]. And ever since, XRD has become one of the most proliferous techniques to quantify the phases in multiphase crystals [14]. Earlier, phase quantification was analysed based on the comparison of a single or sets of reflection peaks with standard patterns [15] (Reference Intensity Ratio (RIR), Internal Standard (IS)), but with the rise of full-pattern fitting methodologies (Rietveld method) [16, 17], complete experimental pattern can be fitted against a model profile by integrating the physical parameters of identified crystal structure [18].

Over the last few decades, the advancement of computer technology has enabled diffractionists to work with the whole XRD pattern rather than working with relative intensities of a few identified peaks as done in RIR and IS methods. The basic approach in a Rietveld method is to obtain the best XRD data, identify all the anticipated phases present and input basic structural data of all the phases, and let the computer model our data until the best fit to the experimental XRD pattern is obtained. The method usually involves refinement of a residual between a measured diffraction pattern and a simulated diffraction pattern by applying a least-square approach [13] as follows,

$$R = \sum_i W_i \ (I_{o,i} - I_{c,i})^2$$

where,

R= residual

W_i=1/$I_{c,i}$

$I_{o,i}$= observed intensity at ith step

$I_{c,i}$= calculated intensity at ith step

The simulated XRD pattern is modelled using a large number of parameters, such as crystal structure parameters (atom position, displacement due to thermal vibrations), scale factor to adjust the relative intensities of the reflections, peak profile and background parameters and parameters simulating the instrumental aberrations [16],

$$I_{c,i} = S \sum_K L_K |F_K|^2 \varphi(2\,\theta_i - 2\theta_K) O_K A + I_{b,i}$$

where,

S= scale factor

K= Miller indexes (hkl)

L_K= Lorentz polarization factor for Kth Bragg's reflection

Φ= reflection profile function

O_K= preferred orientation function

A= absorption factor

F_K= structure factor for the K^{th} Bragg's reflection

$I_{b,i}$= background intensity at i^{th} step

Therefore, it is observed that the model parameters considered not only include the atomic positions and thermal vibration factors, but also parameters for the background, the instrumental features and the reflection profile broadening agents. The function to refine multiple phases simultaneously with Rietveld scale factors makes Rietveld refinement probably the most reliable method for quantitative phase analysis in a multiphase crystal [16, 19]. The weight fraction of α phase (W_α) can be obtained using the following equation [14],

$$W_\alpha = \frac{S_\alpha (ZMV)_\alpha}{\sum_{i=1}^{n} S_i \, (ZMV)_i}$$

where,

S_α= refined scale factor of phase α

Z= number of molecules in an unit cell

M= molecular weight (in atomic mass units)

V= unit cell volume ($Å^3$)

n= number of crystalline phases

There are numerous Rietveld analysis software which are available commercially (Topas, Jade, HighScore Plus, *etc*) or free of cost (GSAS, Full Prof, Maud, *etc*). We have used GSAS (General Structure Analysis System) software for our quantitative phase analysis because primarily it is free and among all the free softwares, it has the most simple user-

interface feature. GSAS [20] can be downloaded from the website http://www.ccp14.ac.uk/solution/gsas/.

The term "refinement" in the Rietveld method refers to the process of fitting the model parameters used, to the closest observed. Hence to access the quality of matching results, some numerical criteria is necessary in order to judge the accuracy of the program. There are several R values which are generated based on different computer softwares used that can be used to evaluate the fit: R-structure factor (R_F), R-Bragg factor (R_B), R-pattern factor (R_p) and the weighted-profile factor (R_w). In our simulation software GSAS, we are considering R_w factor for accurate fit. The R_w is defined as,

$$R_w = \frac{\sum_i W_i \ (I_{o,i} - I_{c,i})^2}{\sum_i W_i \ (I_{o,i})^2}$$

where,

$W_i = 1/I_{c,i}$

$I_{o,i}$ = observed intensity at i^{th} step

$I_{c,i}$ = calculated intensity at i^{th} step

2.3.4. Procedure for X-Ray Diffraction

X-ray powder patterns were obtained using monochromated Cu-Kα radiation (λ=1.54178 Å) on a Bruker Proteum diffraction system equipped with Helios high-brilliance multilayer optics, a Platinum 135 CCD detector and a Bruker Microstar microfocus rotating anode X-ray source operating at 45 kV and 60 mA. The scanning was done from 10-90° (2θ) with step size of 0.5°. Figure 2.10 shows the Bruker diffractometer located at Structural Biology Center (SBC), West Campus, The University of Kansas.

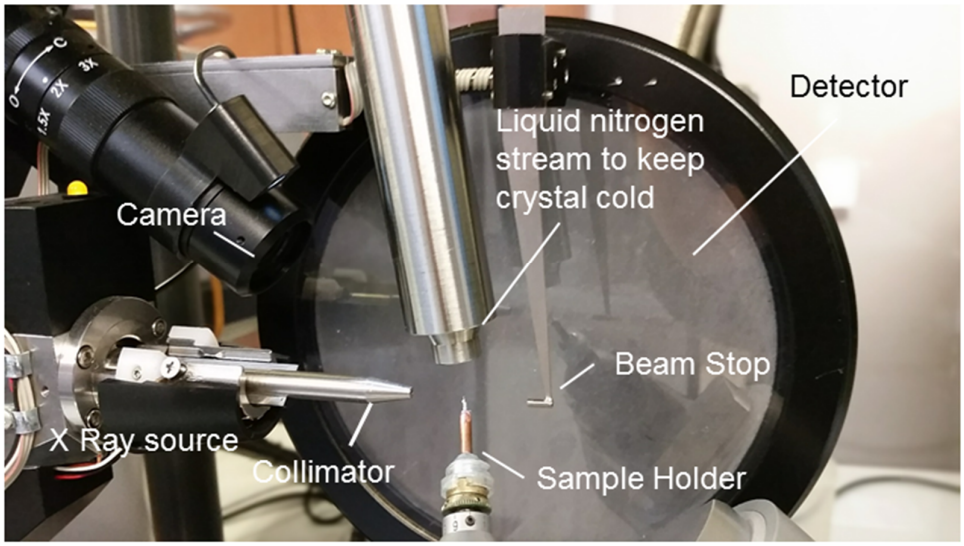

Fig. 2.12. Bruker Proteum diffractometer

To prepare the sample for XRD analysis, the Rh_xS_Y/C catalyst powders were mixed with a small amount of paratone-N oil to form a paste that was placed in a small (<0.5 mm) nylon kryoloop and mounted on the goniometer head. Figure 2.11 shows a sample holder.

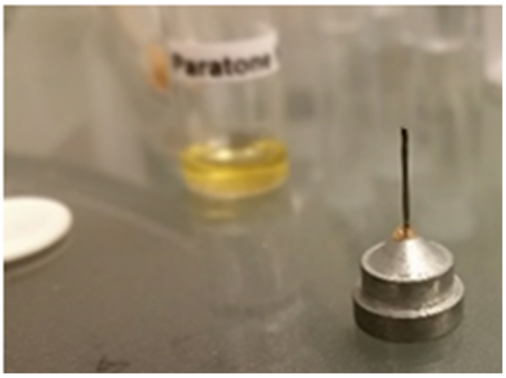

Fig. 2.13. Sample holder for Bruker diffractometer

Two overlapping 1 min 180° Θ-scans were collected using the Bruker Apex2 V2010.3-0 software package with the detector at 2 θ =10° to 90° using a sample-to-sample detector distance of 50 mm. These overlapping scans were merged and converted to a xxx.raw file using the Pilot/XRD2 evaluation option that is part of the APEX2 software

package. This xxx.raw file was then processed using the Bruker EVA powder diffraction software package.

2.3.5. Procedure to Perform Rietveld Refinement in GSAS-II Software

The steps followed by Nirala *et al.* [21] to perform the Rietveld analysis in GSAS software on Rh_xS_y/C electrocatalyst were implemented. They are as follows,

1) Double click on GSASII.py icon on the desktop.

2) Three windows will pop out – GSASII plots, GSAS-II data tree and GSAS-II data display.

3) Go to the GSAS-II data tree window and import the XRD data file. This can be done by '*Import/Powder Data/fromGSAS powder data file'*.

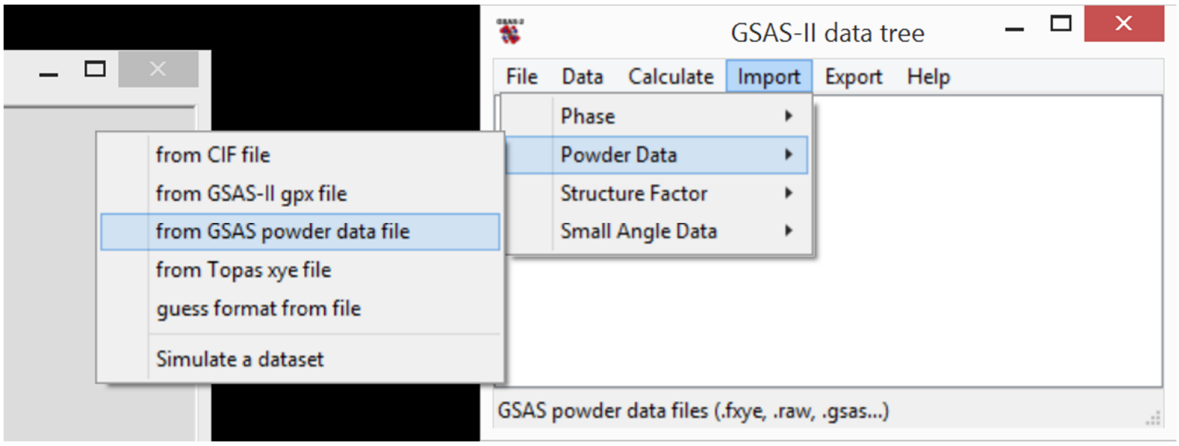

It should be noted that the file need to be saved in xxx.gsas format. Usually the files from Bruker diffractometer is of xxx.raw format. The xxx.raw format can be converted to xxx.gsas format using "PowDLL convertor" software which is available online free of cost.

4) Choose your xxx.gsas file from your specified folder. A window will pop out asking "Do you want to read this file?" Click Yes.

5) A window will pop out asking instrument parameter file (.prm/.inst). If you have an instrument parameter file select from the respective folder where it is saved, else click cancel for default.

6) Select "Defaults from Cu-Kα lab data" from "Select instrument parameters" pop out window. In our case, the monochromatic beam is radiated from Cu-Kα and its wavelength is 1.54 Å, therefore select Cu-Kα.

7) Open the Crystallographic Information File (CIF) of Rh, $Rh_{17}S_{15}$, Rh_3S_4 and Rh_2S_3 phases by clicking "Import/Phase/from CIF file/filename.cif" for each. The CIF files can be downloaded from ICSD database (Inorganic Crystal Structure Database) Rh- ICSD 426969, $Rh_{17}S_{15}$- ICSD 410838; Rh_3S_4 – ICSD 410813 and Rh_2S_3- ICSD 15344.

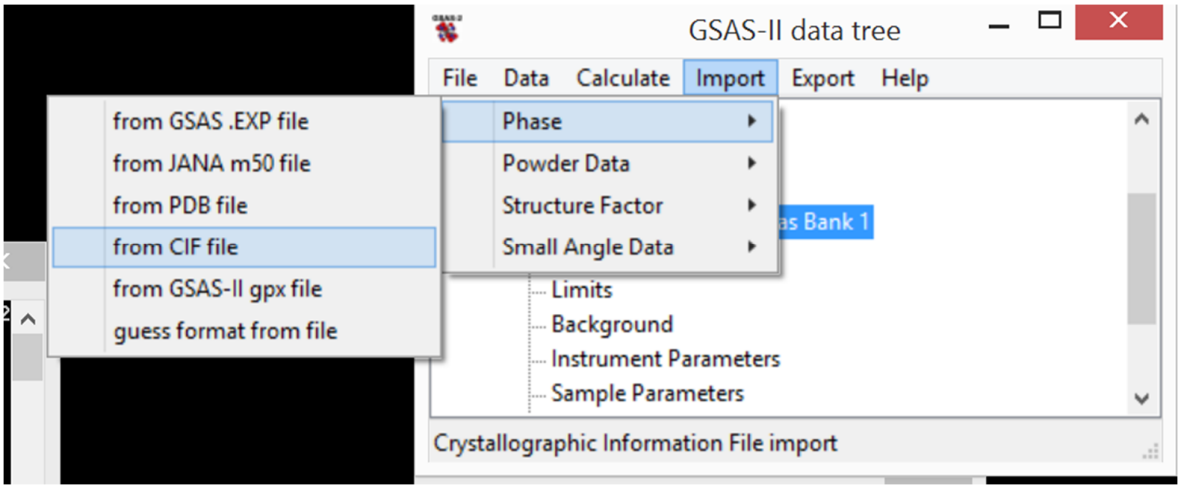

8) To add the selected CIF file for refinement, for *e.g.* Rh, click on the Phase/Rh/Data/ and check "Show filename.gsas bank". Select the other phases.

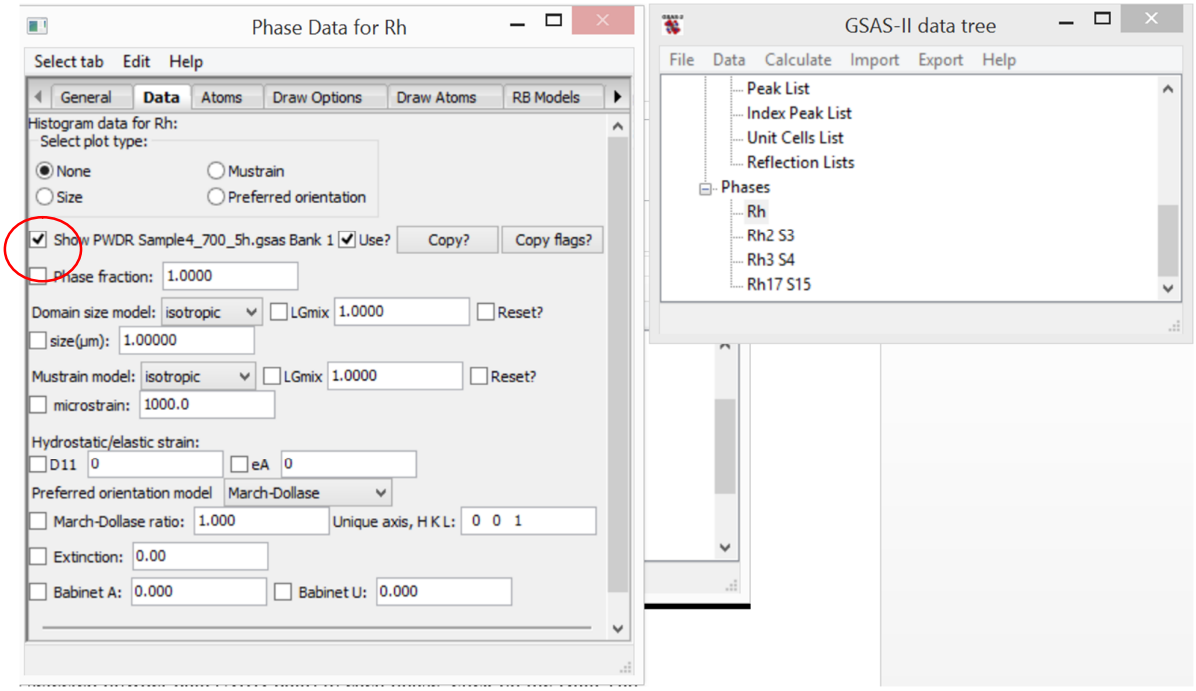

9) After adding the selected XRD data to each phase, click on Background and change the background function to “log interpolate” and no of coefficients to “9”.

10) Run the first refinement by clicking Calculate/Refine.

The project needs to be saved before making any refinements. Save it to your desired folder.

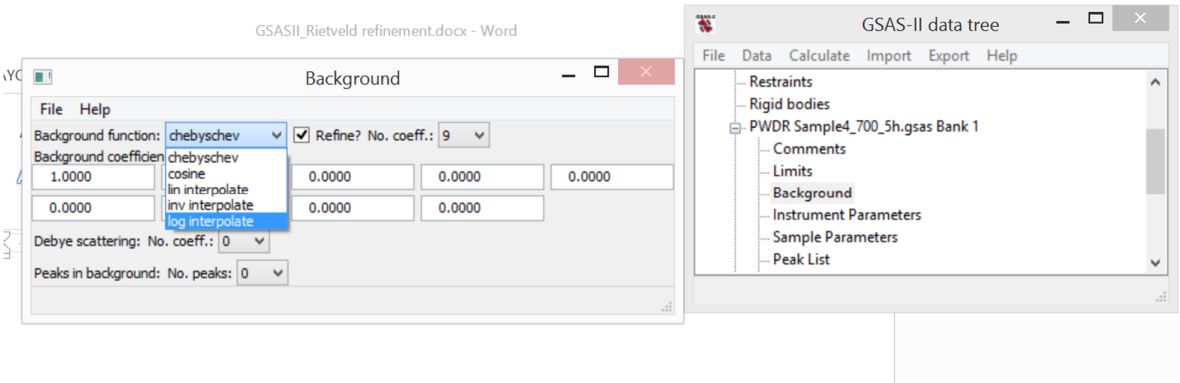

After the first refinement, it will ask for “Load results”. Click OK. Check Refinement value R_w.

11) Instrument parameter refinement is done by selecting Instrument Parameter and checking U and W. Calculate/refine.

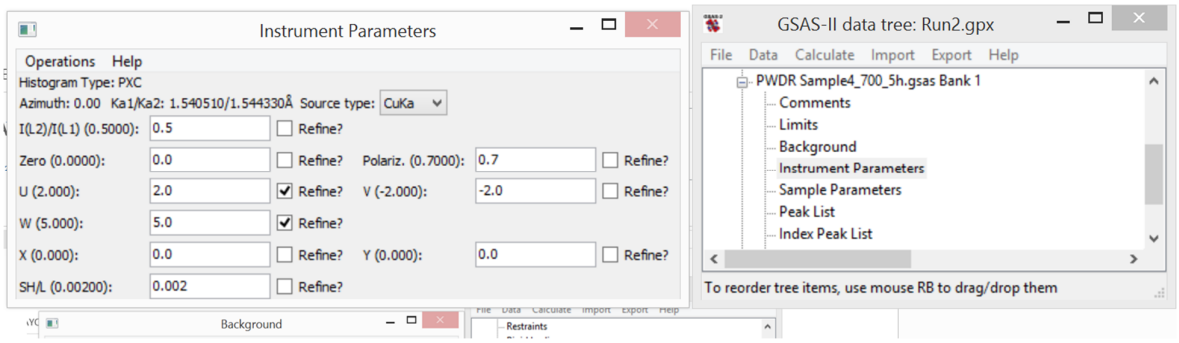

12) Check "Histogram Scale factor" and "X sample displacement perpendicular to beam" under Sample Parameters. Calculate/refine.

13) Check "Refine Unit Cell" and "Phase fraction" for each phase. Calculate/Refine.

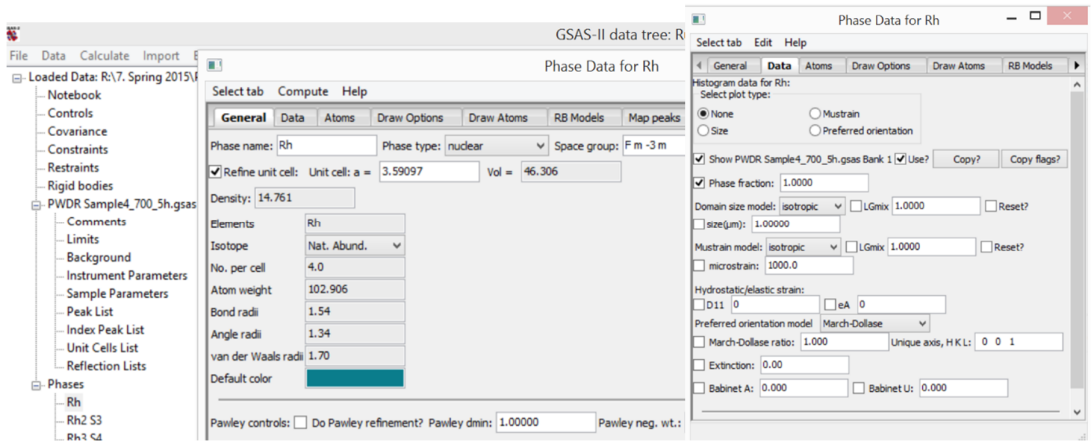

14) A general rule of thumb is the value of R_w less than 10 % is a good fit. The refinement is continued until R_w value is less than 10 %. Once the above refinements are completed, search for 'weight fraction' in filename.lst file which would be generated in the same folder where the computation was performed. The weight fraction of each phases will be displayed in the filename.lst file. Record it.

Using these steps in GSAS program, the accuracy of our approach was verified first by running a quantitative phase analysis on a commercial RhxSy/C catalyst (BASF Inc). In our simulation result, it was found that commercial catalyst is ≈ 99 % pure $Rh_{17}S_{15}$ with minimum amount of Rh_2S_3 and Rh_3S_4 as previously reported by Nirala *et al.* [21].

2.4. REFERENCES

1. Allen, R.J. and A.F. Gulla, *Synthesis of noble metal, sulphide catalysts in a sulfide ion-free aqueous environment*. 2005, Google Patents.
2. Cao, D., et al., *Oxygen Reduction Reaction on Ruthenium and Rhodium Nanoparticles Modified with Selenium and Sulfur.* Journal of The Electrochemical Society, 2006. **153**(5): p. A869-A874.
3. Gullá, A.F., et al., *Carbon-supported low-loading rhodium sulfide electrocatalysts for oxygen depolarized cathode applications.* Applied Catalysis A: General, 2007. **326**(2): p. 227-235.
4. Ziegelbauer, J.M., et al., *Chalcogenide electrocatalysts for oxygen-depolarized aqueous hydrochloric acid electrolysis.* Electrochimica Acta, 2007. **52**(21): p. 6282-6294.
5. Allen, R.J., et al., *Rhodium electrocatalyst and method of preparation*. 2000, Google Patents.
6. Masud, J., et al., *A RhxSy/C Catalyst for the Hydrogen Oxidation and Hydrogen Evolution Reactions in HBr.* Journal of The Electrochemical Society, 2015. **162**(4): p. F455-F462.
7. Srinivasan, S., et al., *Advances in solid polymer electrolyte fuel cell technology with low platinum loading electrodes.* Journal of Power Sources, 1988. **22**(3–4): p. 359-375.
8. Wilson, M.S. and S. Gottesfeld, *Thin-film catalyst layers for polymer electrolyte fuel cell electrodes.* Journal of Applied Electrochemistry, 1992. **22**(1): p. 1-7.

9. Doña Rodríguez, J.M., J.A. Herrera Melián, and J. Pérez Peña, *Determination of the Real Surface Area of Pt Electrodes by Hydrogen Adsorption Using Cyclic Voltammetry.* Journal of Chemical Education, 2000. **77**(9): p. 1195.

10. Gilman, S., *Multipulse potentiodynamic studies of the adsorption of carbon monoxide and hydrogen on rhodium electrodes. II. Mixed adsorption of carbon monoxide and hydrogen.* The Journal of Physical Chemistry, 1967. **71**(13): p. 4339-4343.

11. A.J. Bard, L.R.F., *Electrochemical Methods: Fundamentals and Applications*. 2001, New York: John Wiley.

12. Yang, L., *Synthesis and optical properties of ZnO nanostructures*. 2008, Linkoping University.

13. Clark, G.L. and D.H. Reynolds, *Quantitative analysis of mine dusts: An X-ray diffraction method.* Industrial & Engineering Chemistry Analytical Edition, 1936. **8**(1): p. 36-40.

14. Ruben SNELLINGS, L.M., Gilles MERTENS & Jan ELSEN, *Rietveld refinement strategy for quantitative phase analysis of partially amorphous zeolitized tuffaceous rocks.* Geologica Belgica [En ligne], 2010. **13**(3): p. 182-196.

15. Harold P. Klug, L.E.A., *X-Ray Diffraction Procedures: For Polycrystalline and Amorphous Materials*. 1974, Wiley-VCH. p. 992.

16. Young, R.A., *The Rietveld method*. 1993, New York: Oxford University Press.

17. Antonio, S.G., et al., *Quantitative phase analyses through the rietveld method with X-ray powder diffraction data of heat-treated carbamazepine form III.* Journal of Pharmaceutical Sciences, 2011. **100**(7): p. 2658-2664.

18. Guirado, F., S. Galí , and S. Chinchón,*Quantitative Rietveld analysis of aluminous cement clinker phases.* Cement and Concrete Research, 2000. **30**(7): p. 1023-1029.

19. Patrizi Canton, P.F.F., Carlo Meneghini, Alvise Benedetti, Giulio Pozzi, *Nanoscale Characterization of Metal Nanoclusters by Means of X-Ray Diffraction (XRD) and Transmission Electron Microscopy (TEM) Techniques*, in *Metal Nanoclusters in Catalysis and Materials Science-The Issue of Size Control*. 2008, Elsevier. p. 129–147.

20. Dreele, A.C.L.a.R.B.V., *General Structure Analysis System (GSAS)*. 1994, Los Alamos National Laboratory.

21. Singh, N., et al., *Investigation of the Electrocatalytic Activity of Rhodium Sulfide for Hydrogen Evolution and Hydrogen Oxidation*. Electrochimica Acta, 2014. **145**(0): p. 224-230.

CHAPTER 3
RESULTS AND DISCUSSION

This chapter will give an overview of the phase composition and electrochemical characterization of the rhodium sulfide catalyst supported on high surface area carbon (Rh_xS_y/C) heat treated at 650°C (C1), 660°C (C2) , 670°C (C3), 680°C (C4), 690°C (C5) and 700°C (C6). The chapter is organised as follows. Section 3.1 discusses the result of equilibrium phase composition of catalysts C1-C6 obtained by using XRD analysis and Rietveld technique. Section 3.2 will give an overview of electrochemical characterization *i.e.* electrochemical active surface area (ECSA) and hydrogen oxidation reaction/ hydrogen evolution reaction (HOR/HER) exchange current density (i_0) of the synthesized catalysts in an RDE setup.

3.1. EQUILIBRIUM PHASE COMPOSITION

3.1.1. Variation of Phase Composition with Reaction Time

A phase is a homogeneous portion of a system that has its uniform physical and chemical characteristics. Phase equilibrium is reached in a multiphase crystal when the composition of its constituent phases does not vary with reaction time.

Hence, an initial study was made to obtain a phase equilibrium of Rh_xS_y/C catalyst versus reaction time at final temperatures. Starting with heat-treatment at 700°C, Rh_xS_y/C catalysts were synthesized by thermally reducing the precursor for 1, 2, 3 and 5 h to see the variation of phase composition with reaction time and in the process find out the time to obtain phase equilibrium at 700°C. Catalysts were collected and XRD patterns were obtained

in the Bruker diffractometer. For every reaction time (t), XRD patterns were collected for 3 different samples and quantitative phase analysis using the Rietveld method was performed on each sample to see the uniformity in the composition of the catalyst.

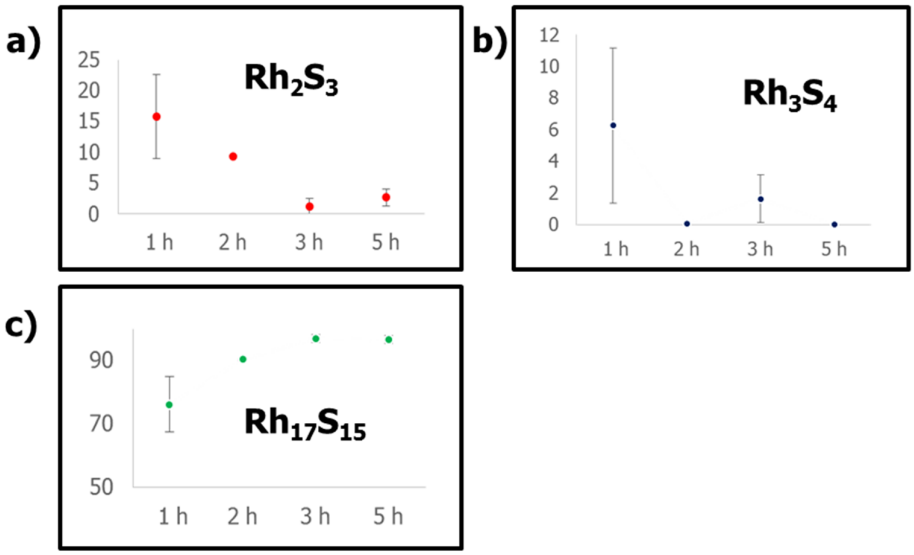

Fig. 3.1. Weight composition of catalyst C6 heat treated for 1, 2, 3 and 5 h. y-coordinate represents the weight percentage of a)Rh_2S_3 b) Rh_3S_4 and c) $Rh_{17}S_{15}$ along time (hour) in x-coordinate. Very trace amount of Rh (<1%) was observed.

From Figure 3.1, it can be concluded that phase equilibrium was not attained at 1 h and 2 h since increasing the reaction time from 1h → 2 h → 3h, reactions were still observed to be undergoing as $Rh_{17}S_{15}$ phase increases from ~ 90% to ~ 97% (2 h → 3 h) and Rh_2S_3 decreases from ~ 9% to ~ 2% (2 h→ 3 h). But analysis of the phase composition at 3 h and 5 h suggests a phase equilibrium in the system, as all the Rh_2S_3 (~2%) were converted to Rh_3S_4 and $Rh_{17}S_{15}$ and near pure phase $Rh_{17}S_{15}$ (~97%) was observed in both cases of 3 h and 5 h. No significant percentages of Rh (<1 %) metal was observed at 690-700°C which concludes that Rh metal starts to form at about 690 °C.

At higher temperature (700°C), it is known that equilibrium will be attained faster than at low temperature (650°C) as rate constant of a reaction depends on temperature; hence

Rh_xS_y/C was synthesized at 650°C for longer times, 3 h (C1-3), 4 h (C1-4) and 5 h (C1-5) to find out its reaction time for phase equilibrium. XRD patterns were obtained and quantitative phase analysis by Rietveld refinement was done on the samples as it was done before with the 700°C samples. Figure 3.2 shows the phase composition of C1-3, C1-4 and C1-5.

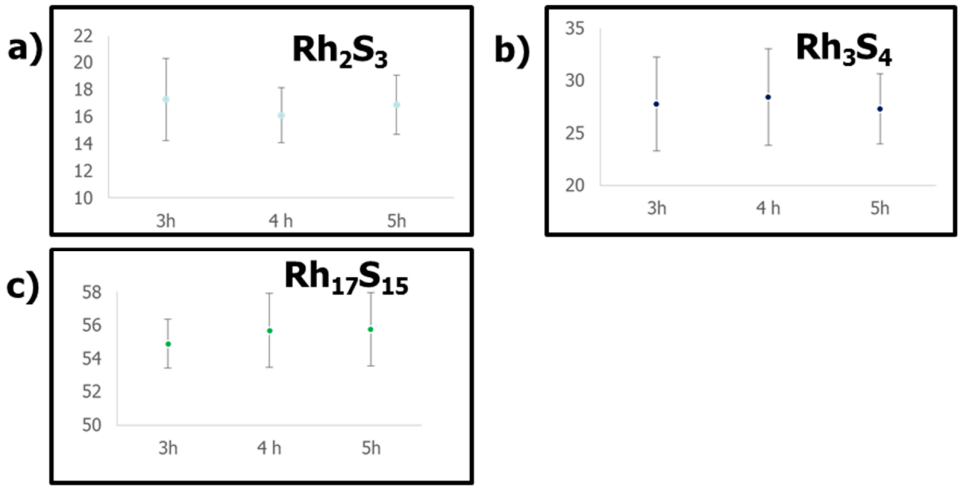

Fig. 3.2. Weight composition of Rh_xS_y/C catalyst heat treated at 650°C for 3, 4 and 5 h. y-coordinate represents the weight percentage of a) Rh_2S_3 b) Rh_3S_4 and c) $Rh_{17}S_{15}$ along time (hour) in x-coordinate. No Rh was observed at 650°C.

An analysis of the weight fractions of Rh_xS_y phases at different reaction time as shown in Figure 3.2 summarizes that no significant changes in the composition was observed for C1-3, C1-4 and C1-5 catalysts. Hence, a phase equilibrium was observed at 3 h for catalyst HT at 650°C.

3.1.2. Equilibrium Phase Composition of Rh_xS_y/C Catalyst

From Section 3.1.1 it was concluded that phase equilibrium is attained at 3 h for Rh_xS_y/C catalyst C1, C2, C3, C4, C5 and C6 and hence all the catalyst were thermally reduced for 3 h at their respective temperatures inside a quartz-tube furnace. XRD analysis and quantitative phase composition using GSAS-II was performed on the samples. Table 3.1 summarizes the phase composition along with the standard deviations (SD) observed for each

phase and a graph was plotted as shown in Figure 3.a. An equilibrium phase diagram is shown in Figure 3.3.b.

Table 3.1 Results of the Rietveld refinement of catalysts C1-C6.

Catalyst	**Rh_2S_3**		**Rh_3S_4**		**$Rh_{17}S_{15}$**	
	%	S.D	%	S.D	%	S.D
C1	28.4	2.9	13.5	3.4	58.1	1.4
C2	26.9	2	15.6	2.9	57.5	0.9
C3	23.6	1.2	9.0	1.7	67.4	3.4
C4	21.3	1.9	8.9	0.7	69.8	1.3
C5	2.3	2.3	1	1.4	96.7	1.8
C6	1.2	1.3	1.6	1.5	97.2	1.3

From Table 3.1, there is a clear trend being observed in weight percentages of the phases as we go from 650°C to 700°C. As T is increased from 650°C to 670°C, small amounts of Rh_2S_3 and Rh_3S_4 transforms to $Rh_{17}S_{15}$ phase by loss of sulfur and attains equilibrium in the system with reaction time. With further increase in T, the percentage of conversion is high and almost all the Rh_2S_3 and Rh_3S_4 phases transform to $Rh_{17}S_{15}$ phase (~97%) thereby attaining a phase equilibrium in the multiphase crystal system after 3 h.

A recent study by Masud *et al.* showed the percentage composition of Rh_2S_3, Rh_3S_4, $Rh_{17}S_{15}$ and Rh to be 17%, 15%, 52% and 16% respectively by XPS analysis in Rh_xS_y/C catalyst HT at 800°C for 30 min. Although this catalyst might not have attained phase equilibrium, the result is in good agreement with our XRD results where we have seen the Rh_2S_3 phase weight percentage decrease as the temperature is increased from 650°C to 700°C to form Rh_3S_4 and $Rh_{17}S_{15}$ phase; and Rh metal starts to form at about 690°C and its

percentage increases with elevation in temperature by release of S from the phases of rhodium sulfide.

a)

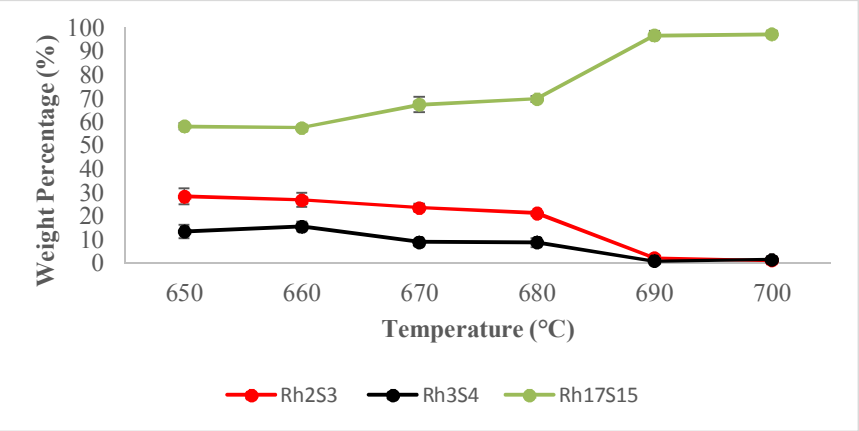

b)

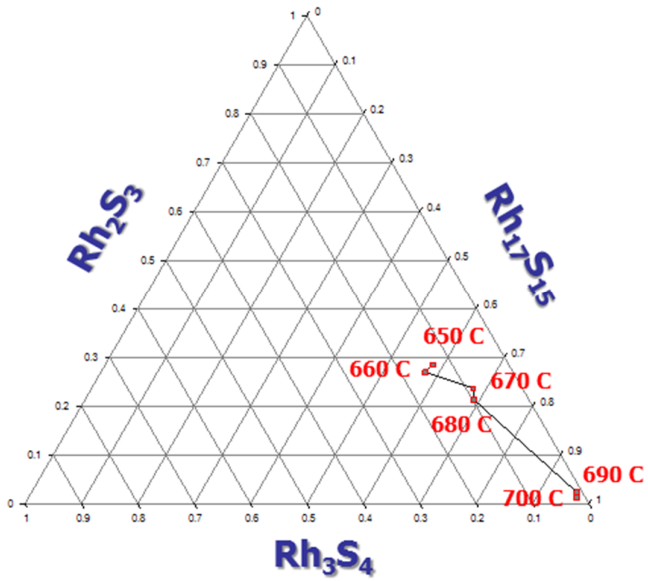

Fig. 3.3. (a) Equilibrium phase composition of Rh_xS_y/C catalyst HT at 650°C, 660°C, 670°C , 680°C, 690°C and 700°C for 3 h. (b) Ternary plot of the equilibrium phase composition at inert gas atmosphere

3.2. ELECTROCHEMICAL STUDY

3.2.1. Electrochemical Active Surface Area (ECSA) Calculation

ECSA was calculated by performing a CV from 0.0 V to 0.425 V vs SHE at a scan rate of 10 mV/s to avoid the oxidation of the materials at higher potentials that use to lead to inconsistent ECSA measurements [1]. Figure 3.4 shows the CVs of the catalyst C1, C2, C3, C4, C5 and C6 in N_2- saturated 1 M H_2S0_4 solution at RT.

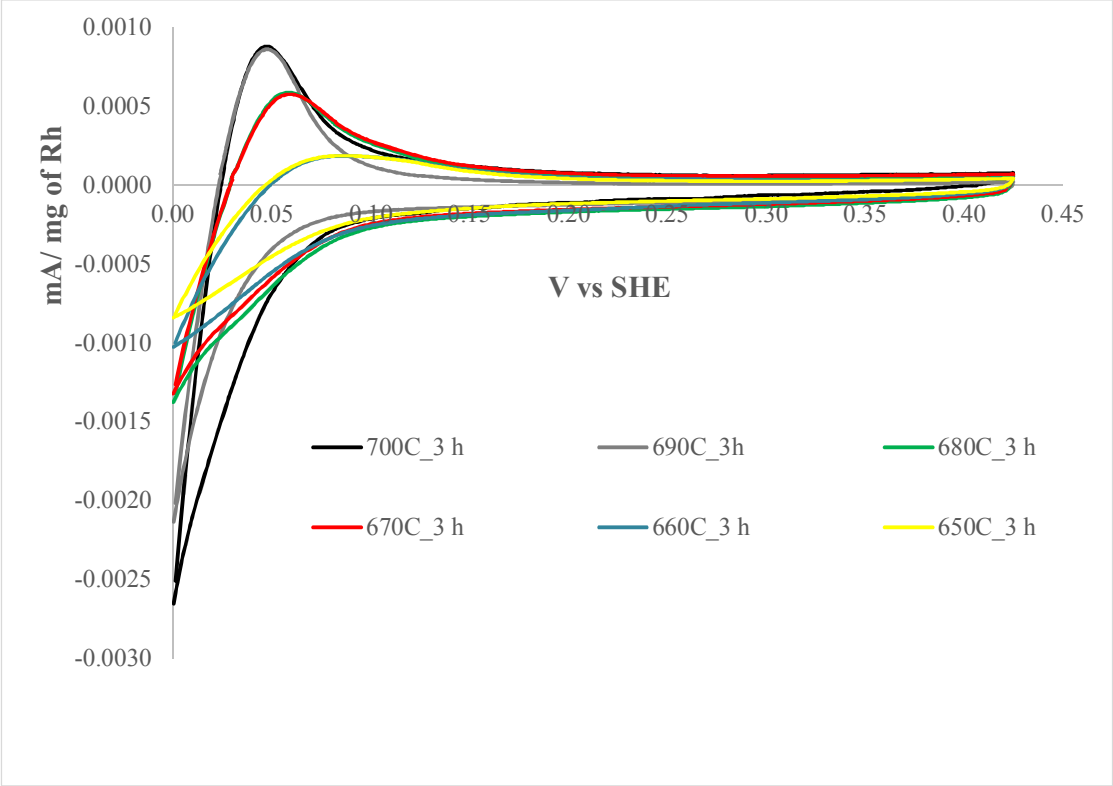

Fig. 3.4. CVs of catalyst C1, C2, C3, C4, C5 and C6 in N_2-saturated 1 M H_2SO_4

As previously reported in the literature [1-3], the activity of semiconductor Rh_2S_3 phase towards HOR/HER reaction is less as compared to the metallic phases Rh_3S_4 and $Rh_{17}S_{15}$ and it is evident from our ECSA measurements. Table 3.2 summarizes the ECSAs of catalyst C1 to C6 HT for 3 h.

Table 3.2. ECSA of catalyst C1, C2, C3, C4, C5 and C6 HT for 3 h.

Catalyst	ECSA (m^2/mg Rh)
C1	3.4
C2	3.3
C3	5.2
C4	5.4
C5	8.1
C6	8.7

The highest ECSAs were obtained for catalysts C5 and C6 HT for 3h which is in good agreement with our XRD results which showed that they contained the lowest weight percent of inactive phase (Rh_2S_3).

3.2.2. HOR/HER Exchange Current Density Calculation

Exchange current density is an intrinsic property of any catalyst. In our case of multiphase phase electrocatalyst, the exchange current density will be contributed from all the active phases. Figure 3.5 shows a linear plot between current (I) versus applied potential of catalysts a) C1, C3 and C5 and b) C2, C4 and C6 each HT for 3h, obtained from RDE experiments.

a)

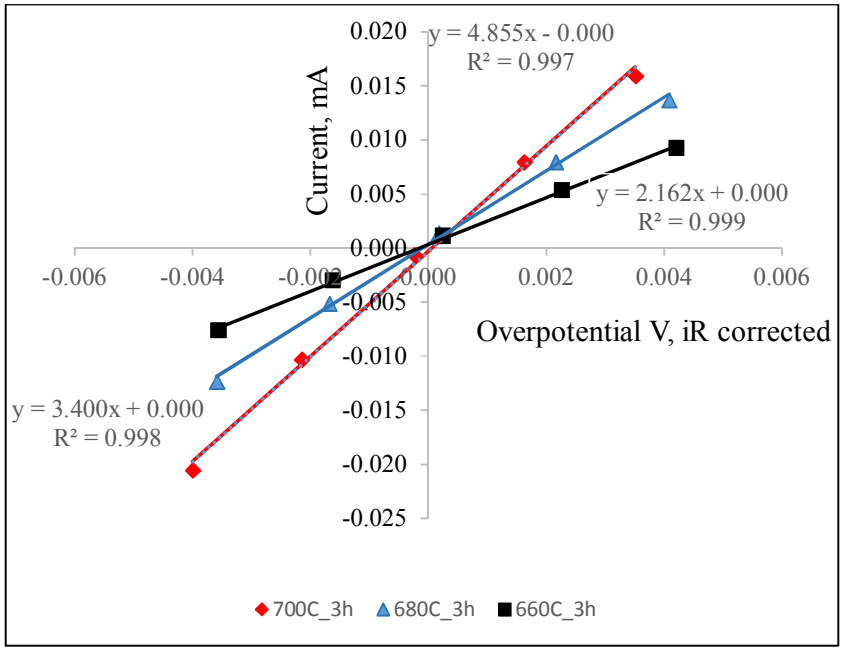

b)

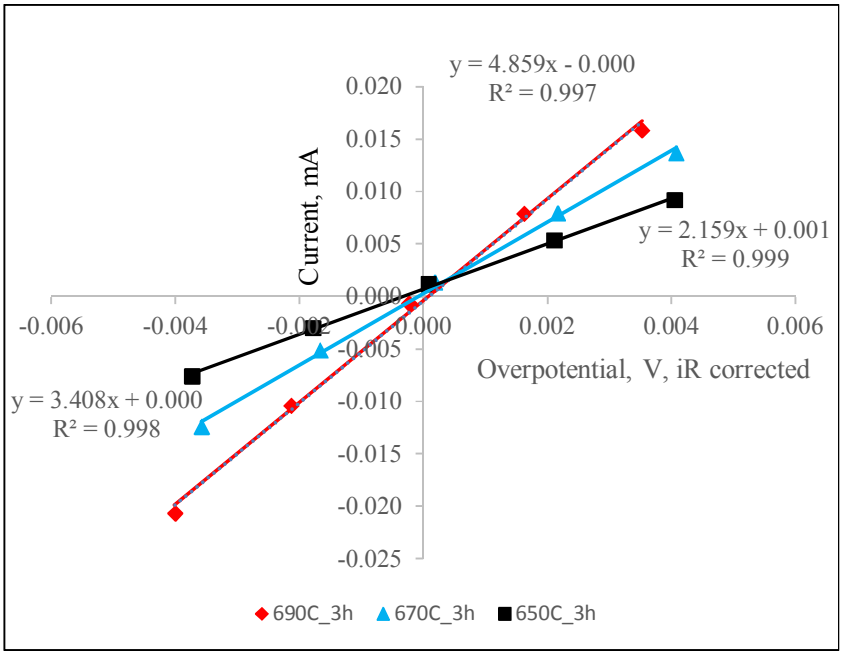

Fig. 3.5. Linear plots of current versus overpotential (iR corrected) of catalysts a) C1, C3 and C5 and b) C2, C4 and C6.

Table 3.3. HOR/HER exchange current density of catalysts C1-C6 HT for 3 h in 1 M H_2SO_4

Catalyst	i_o (mA/cm^2)	i_o* (mA/mg of Rh)
C1	0.36	11.56
C2	0.38	34.37
C3	0.43	38.73
C4	0.44	40.81
C5	0.59	47.79
C6	0.6	52.20

Based on the higher ECSAs and activities of the mixture containing lower amount of Rh_2S_3 phase, it is observed that the activity of the Rh_xS_y/C catalysts increase with increased amount of active Rh_3S_4 and $Rh_{17}S_{15}$ phases which is in good agreement with our XRD results.

Table 3.4. Summary of the phase composition, ECSA and activity of the catalysts C1-C6 HT for 3 h.

Catalyst	Rh_2S_3	Rh_3S_4	$Rh_{17}S_{15}$	ECSA (m^2/mg Rh)	Activity (mA/cm^2)
C1	28.4±2.9	13.5±3.4	58.1±1.4	3.4	0.34±0.04
C2	26.9±2	15.6±2.9	57.5±0.9	3.3	0.35±0.04
C3	23.6±1.2	9.0±1.7	67.4±3.4	5.2	0.41±0.02
C4	21.3±1.9	8.9±0.7	69.8±1.3	5.4	0.43±0.03
C5	2.3±2.3	1±1.4	96.7±1.8	8.1	0.57±0.06
C6	1.2±1.3	1.6±1.5	97.2±1.3	8.7	0.59±0.06

3.3. REFERENCES

1. Masud, J., et al., *A RhxSy/C Catalyst for the Hydrogen Oxidation and Hydrogen Evolution Reactions in HBr.* Journal of The Electrochemical Society, 2015. **162**(4): p. F455-F462.
2. Singh, N., et al., *Investigation of the Electrocatalytic Activity of Rhodium Sulfide for Hydrogen Evolution and Hydrogen Oxidation.* Electrochimica Acta, 2014. **145**(0): p. 224-230.
3. Singh, N., et al., *Investigation of the Active Sites of Rhodium Sulfide for Hydrogen Evolution/Oxidation Using Carbon Monoxide as a Probe.* Langmuir, 2014. **30**(19): p. 5662-5668.

CHAPTER 4
CONCLUSION AND RECOMMENDATION

4.1. CONCLUSION

In this work, I have successfully synthesized rhodium sulfide electrocatalyst supported on high surface area carbon by refluxing rhodium chloride ($RhCl_3$) with ammonium thiosulfate ($(NH_4)_2S_2O_3$) and thermally reducing it in Argon (Ar) atmosphere from temperatures 650°C-700°C. An equilibrium phase composition of different phases of rhodium sulfide catalyst was computed using X-ray Diffraction (XRD) and Rietveld analysis to provide an insight into the phase composition/activity relationship of these electrocatalysts. The active area and hydrogen oxidation and reduction reaction (HOR/HER) activity of the synthesized catalysts were calculated using a rotating disk electrode (RDE) approach in a conventional three-electrode electrochemical cell.

As observed, the rhodium sulfide electrocatalyst is a mixture of different crystalline phases which comprised of Rh_2S_3, Rh_3S_4, and $Rh_{17}S_{15}$ and some amount of Rh metal. XRD analysis supported the transition of Rh_2S_3 phase to Rh_3S_4 and $Rh_{17}S_{15}$ by sulphur release at elevated temperatures. Thus, in order to obtain pure phase $Rh_{17}S_{15}$, the temperature and reaction time during the thermal reduction should be carefully controlled. Furthermore, our equilibrium phase diagram could provide a potential guide to synthesize rhodium sulfide electrocatalyst tailored to the need of a system.

The most active among the synthesized catalyst for HOR/HER was observed to contain maximum $Rh_{17}S_{15}$ phase at 690 -700°C temperature range. Although the activity of the Rh_xS_y/C catalyst can be increased by increasing the Rh metal concentration at elevated temperatures (> 700°C), but it is not ideal for a H_2-Br_2 fuel cell system due to the instability

of Rh metal in the HBr/Br_2 electrolyte. Hence, to develop the present Rh_xS_y/C catalyst, research should be focussed on improving the efficiency and utilization of the active phases of the Rh_xS_y/C (Rh_3S_4, $Rh_{17}S_{15}$) heat treated at 700°C.

4.2. RECOMMENDATION

From TEM analysis, the present catalyst Rh_xS_y/C heat treated at 700°C for 3 h has particle size on the order of 3-16 nm as shown in the inset of Fig 4.1.

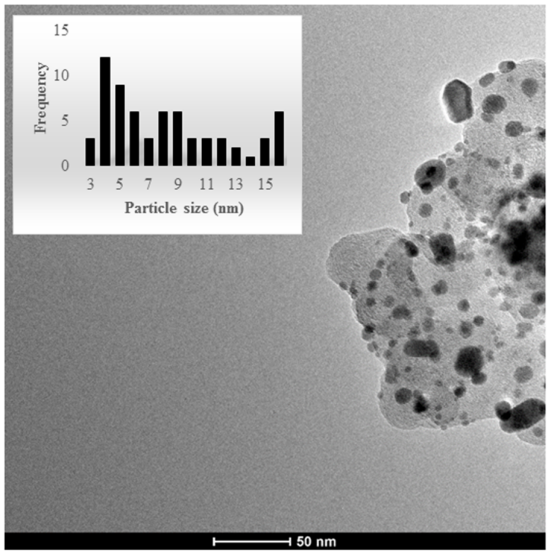

Fig 4.1 TEM image of Rh_xS_y/C catalyst after thermal treatment at 700°C for 3 h. The histogram of particle-size distribution is plotted in the inset.

The wide range of particle size leads to inconsistent and low gravimetric ECSA of the active phase of rhodium sulfide catalyst. Hence reducing the particle size by introduction of surfactant during the catalyst synthesis process can be the further scope of research to improve the activity of the present catalyst.

The temperature gap can be further minimized to 1-2°C during thermal reduction for better phase composition analysis by using better temperature controlled furnace.

APPENDIX A

A.1. COMPUTATIONAL DATA

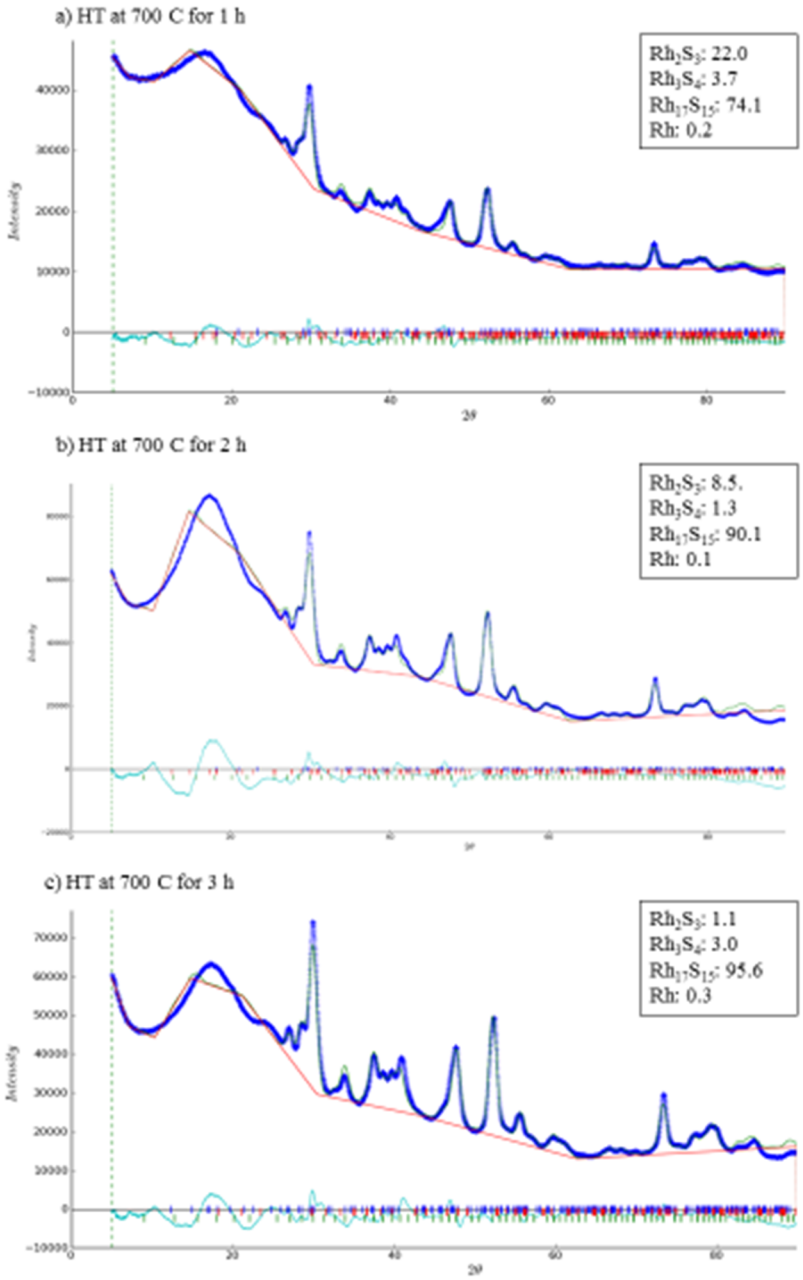

Fig. A.1.1. Rietveld refinement of Rh_xS_y/C catalyst HT at 700°C for a) 1 h b) 2 h and c) 3h. The blue dots represents the experimental data & the green line represents the calculated pattern. The light blue line below is the difference between the calculated and experimental pattern. The red (|) line represents Bragg position of peaks. The base line is represented by (-). The goodness of fit, R_w for each simulation was observed to be <5 %

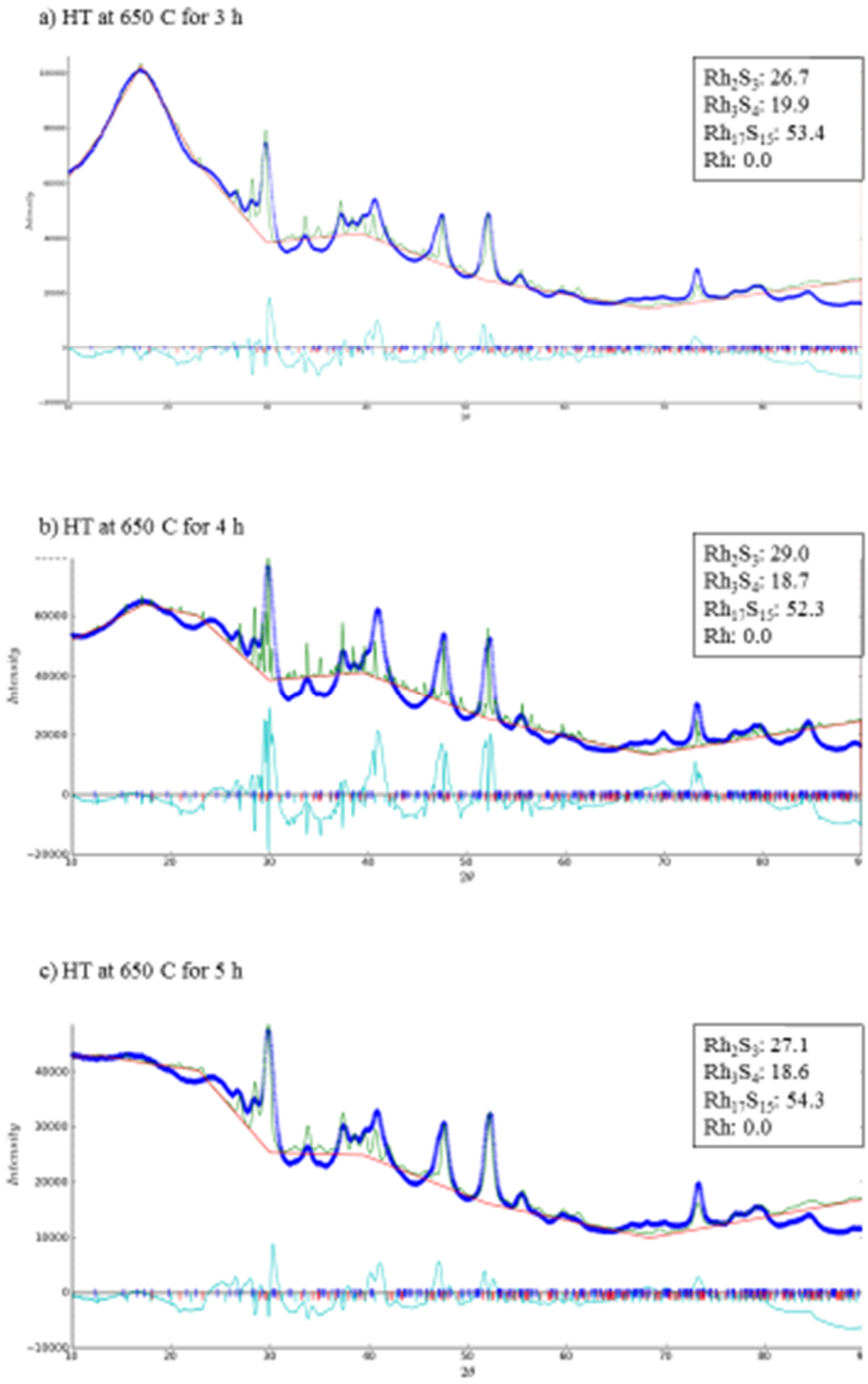

Fig. A.1.2. Rietveld refinement of Rh_xS_y/C catalyst HT at 650°C for a) 3 h b) 4 h and c) 5h. The blue dots represents the experimental data & the green line represents the calculated pattern. The light blue line below is the difference between the calculated and experimental pattern. The red (\|) line represents Bragg position of peaks. The base line is represented by (-).The goodness of fit, R_w for each simulation was observed to be <10 %

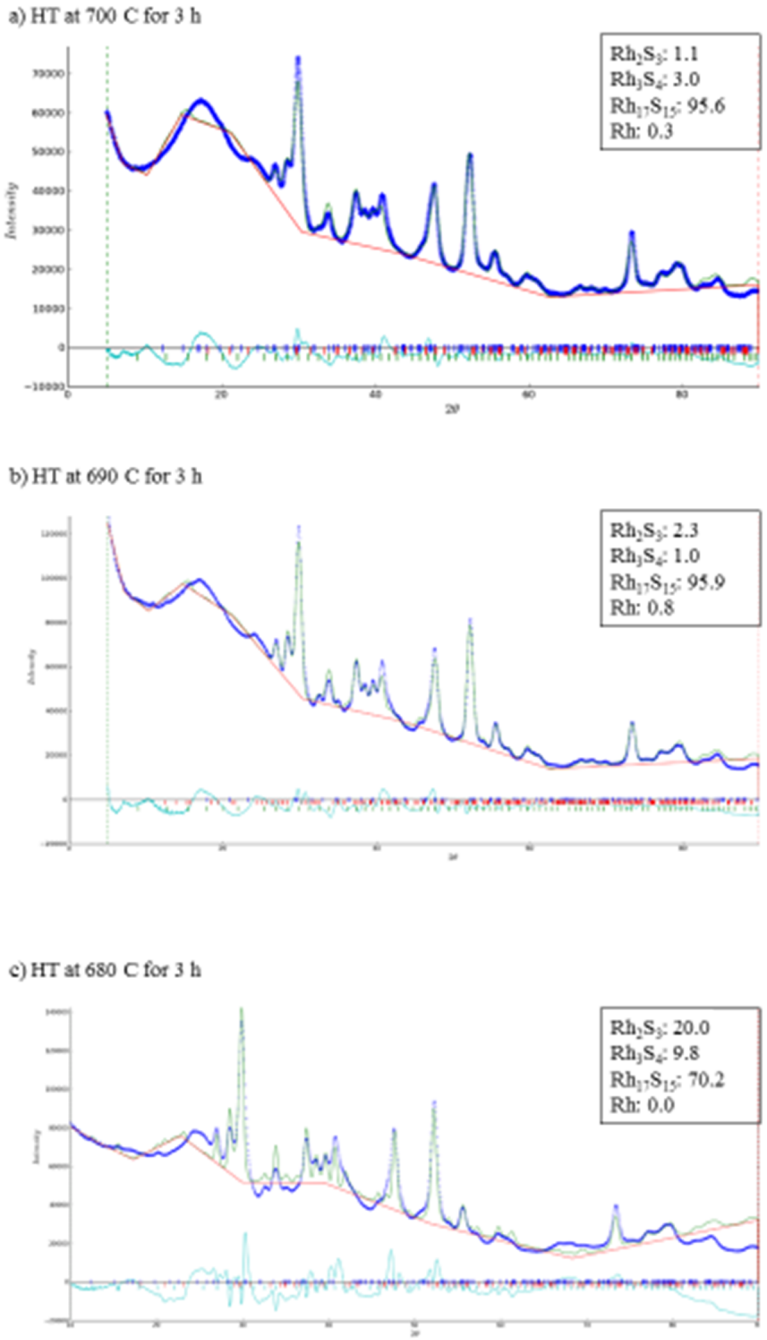

Fig. A.1.3. Rietveld refinement of Rh_xS_y/C catalyst HT for 3 h at a) 700°C b) 690°C and c) 680°C. The blue dots represents the experimental data & the green line represents the calculated pattern. The light blue line below is the difference between the calculated and experimental pattern. The red (|) line represents Bragg position of peaks. The base line is represented by (-).The goodness of fit, R_w for each simulation was observed to be <10 %

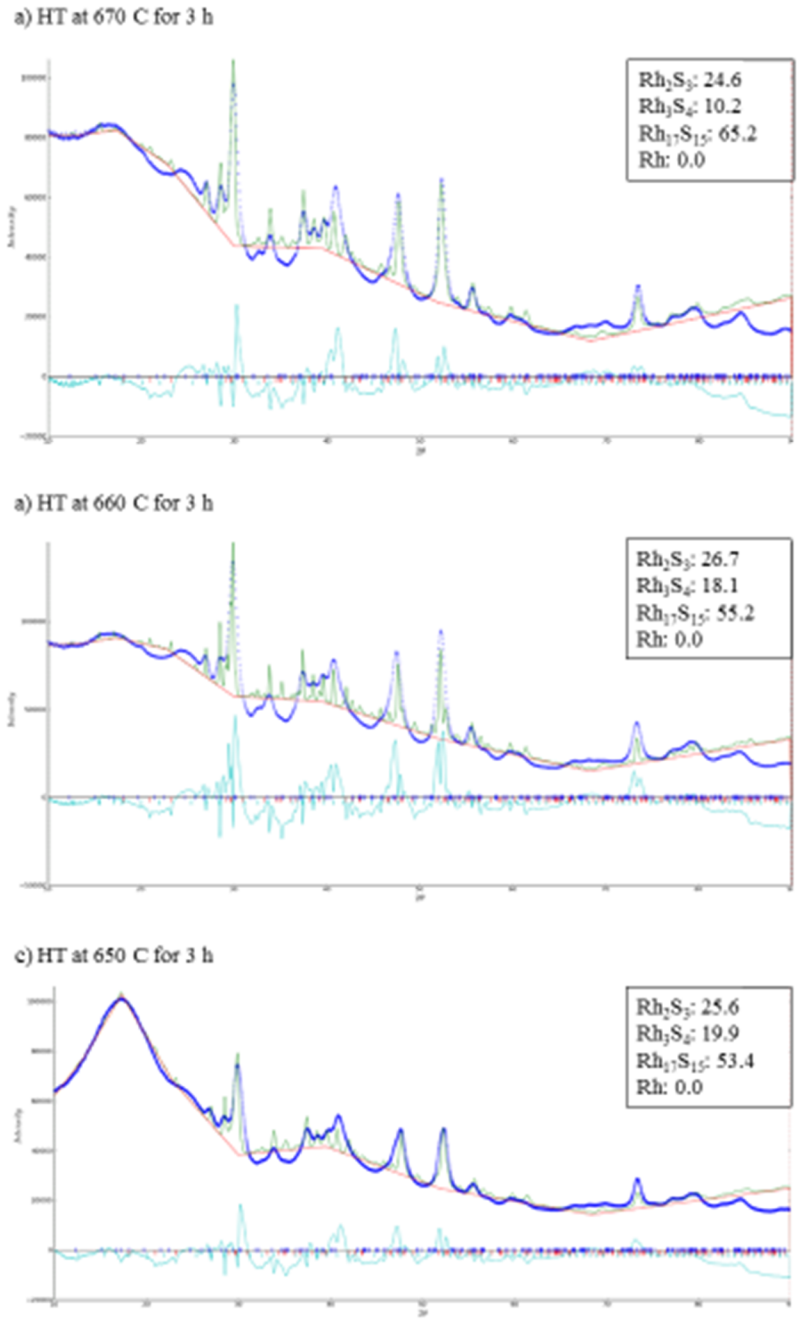

Fig. A.1.4. Rietveld refinement of Rh_xS_y/C catalyst HT for 3 h at a) 670°C b) 660°C and c) 650°C. The blue dots represents the experimental data & the green line represents the calculated pattern. The light blue line below is the difference between the calculated and experimental pattern. The red (|) line represents Bragg position of peaks. The base line is represented by (-).The goodness of fit, R_w for each simulation was observed to be <10 %

A.2 EXPERIMENTAL DATA

Table A.2.1. Experimental data for Fig 3.3.b (Overpotential (η), iR corrected vs Current) for Rh_xS_y/C catalyst heat treated at 700°C, 680°C and 660°C. The resistance, R of the solution varied from 5.6±0.3 Ω.

Rh_xS_y/C catalyst HT for 3 h at	Overpotential (V) (η)	Current (mA) (*i*)	Overpotential (V), iR corrected (η -*i*R)
700°C	-0.0041	-0.0206	-0.0040
	-0.0022	-0.0103	-0.0021
	-0.0002	-0.0006	-0.0002
	0.0017	0.0080	0.0016
	0.0036	0.0159	0.0035
680°C	-0.0037	-0.0124	-0.0036
	-0.0017	-0.0051	-0.0017
	0.0002	0.0014	0.0002
	0.0022	0.0080	0.0022
	0.0042	0.0137	0.0041
660°C	-0.0036	-0.0076	-0.0036
	-0.0016	-0.0030	-0.0016
	0.0003	0.0011	0.0003
	0.0023	0.0053	0.0023
	0.0043	0.0092	0.0042

Table A.2.2. Experimental data for Fig 3.3.a (Overpotential (η), iR corrected vs Current) for Rh_xS_y/C catalyst heat treated at 690°C, 670°C and 650°C. The resistance, R of the solution varied from 5.6±0.3 Ω.

RhxSy/C catalyst HT for 3 h at	Overpotential (V) (η)	Current (mA) (*i*)	Overpotential (V), iR corrected (η-*i*R)
690°C	-0.0041	-0.0207	-0.0040
	-0.0022	-0.0104	-0.0021
	-0.0002	-0.0006	-0.0002
	0.0017	0.0079	0.0016
	0.0036	0.0159	0.0035
670°C	-0.0037	-0.0124	-0.0036
	-0.0017	-0.0051	-0.0017
	0.0002	0.0014	0.0002
	0.0022	0.0080	0.0022
	0.0042	0.0137	0.0041
650°C	-0.0038	-0.0076	-0.0037
	-0.0018	-0.0030	-0.0018
	0.0001	0.0011	0.0001
	0.0021	0.0053	0.0021
	0.0041	0.0092	0.0041

Table A.2.3. Experimental data for Fig 2.6.a. The data shows the variation of temperature (T) with time (t) when the quartz-tube furnace was set for 650°C for 1 h.

Time (min)	Temperature (°C)
1	653.94
2	648.18
3	654.16
4	648.60
5	654.28
6	649.22
7	654.71
8	649.99
9	654.54
10	650.76
11	653.54
12	651.53
13	653.46
14	652.20
15	651.20
16	653.03
17	649.39
18	653.63
19	648.48
20	654.39
21	648.97
22	654.83
23	649.92
24	654.94
25	650.73
26	654.52
27	651.63
28	653.04
29	652.54
30	651.10

Time (min)	Temperature (°C)
31	653.95
32	648.98
33	654.81
34	649.49
35	655.38
36	650.36
37	655.55
38	651.25
39	655.13
40	652.13
41	653.81
42	653.02
43	651.61
44	653.94
45	650.20
46	654.67
47	649.46
48	655.09
49	650.11
50	655.87
51	651.04
52	655.14
53	651.96
54	653.88
55	652.95
56	651.72
57	653.80
58	650.04
59	654.54
60	655.14

Table A.2.4. Experimental data for Fig. 2.6.b. The data shows the variation of temperature (T) with time (t) when the quartz-tube furnace was set for 700°C for 1 h.

Time (min)	Temperature (°C)
1	698.80
2	701.08
3	704.40
4	702.09
5	698.99
6	702.85
7	705.00
8	698.18
9	701.23
10	704.91
11	701.94
12	702.57
13	705.24
14	698.77
15	701.29
16	704.97
17	700.91
18	700.07
19	704.19
20	703.77
21	698.88
22	703.18
23	705.40
24	698.80
25	702.13
26	705.61
27	700.52
28	701.03
29	704.75
30	703.41

Time (min)	Temperature (°C)
31	699.80
32	703.87
33	704.03
34	701.29
35	705.08
36	702.27
37	700.20
38	704.19
39	703.07
40	699.18
41	703.44
42	705.17
43	698.66
44	702.37
45	705.54
46	700.00
47	701.21
48	705.13
49	702.66
50	700.11
51	704.17
52	703.36
53	699.09
54	703.47
55	705.49
56	698.91
57	702.63
58	705.33
59	697.37
60	701.21